Nano Science, Chemistry and Engineering Report

ce.ccerci.ac.ir
Reviews

Corresponding Author Emails:
s.mohammadi@sru.ac.ir
Esmail.doustkhah@istinye.edu.tr
orcid.org/0000-0003-2204-3661
DOI:……...
Keywords:
Density functional theory
Magnetic heterostructures
Photocatalytic water splitting
Electrocatalysis
Strain-engineered catalysis

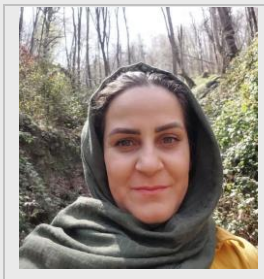
Tailoring Catalytic Activity through Magnetic Interactions, Strain, and External Electric Fields: A First-Principles Perspective

Saeedeh Mohammadi*[a], Esmail Doustkhah*[a,b]

[a] *Clean Energy Research Center (TEAM), Istinye University, Sariyer, Istanbul 34396, Türkiye*
[b] *Chemistry Department, Faculty of Engineering and Natural Sciences, Istinye University, Sarıyer, Istanbul 34396, Türkiye*

Abstract: The rational integration of heterojunctions into photocatalytic water-splitting systems offers a promising route to enhanced catalytic efficiency. However, the vast compositional space of candidate materials and the complexity of interfacial phenomena make the identification of optimal heterojunction pairings a considerable challenge. Density functional theory (DFT) has emerged as an indispensable computational framework for probing the fundamental mechanisms underlying electrocatalytic and photocatalytic processes and for guiding the design of next-generation catalysts. This review surveys the use of DFT in catalyst characterization and performance assessment, with particular focus on magnetic heterostructures, applied external electric fields, and strain engineering. We discuss how DFT provides insight into atomic configurations, electronic structure, interfacial charge redistribution, and reaction Gibbs free-energy changes (ΔG), thereby enabling the elucidation of catalytic mechanisms and the identification of potential rate-determining steps. We further examine the contribution of advanced electronic-structure approaches, namely the GW approximation, the Tran–Blaha modified Becke–Johnson (TB-mBJ) potential, and the Heyd–Scuseria–Ernzerhof (HSE06) hybrid functional, to the accurate prediction of bandgaps and the interpretation of properties pertinent to electro- and photocatalysis. Case studies on the hydrogen evolution reaction (HER), oxygen reduction reaction (ORR), and electrochemical CO_2 reduction reaction (CO_2RR) illustrate how first-principles calculations can map reaction pathways, benchmark catalytic activity, and support rational catalyst design. Rather than an exhaustive survey, this review curates representative examples that bridge computational predictions and experimental findings. Special attention is paid to how magnetic interactions, interface engineering, external electric fields, and lattice strain can be harnessed to modulate electronic structure and tune catalytic behavior. Finally, we address the principal methodological limitations that constrain the accuracy and reliability of DFT-guided catalyst design, and we outline future research directions toward more efficient electrocatalysts and photocatalysts for sustainable energy conversion.

Dr. Saeedeh Mohammadi research interests include density functional theory (DFT), machine learning, and molecular dynamics simulations for the computational design of advanced functional materials. During her research at Shahid Rajaee Teacher Training University, she worked extensively on magnetic materials, particularly layered heterostructures, layered double hydroxides (LDHs), and other low-dimensional systems for energy storage and catalytic applications. She has also collaborated with researchers at Istinye University on the computational design of electro- and photocatalysts using DFT and machine learning, with a particular emphasis on magnetic and layered materials. Her current research interests include computational materials science, electrocatalysis, photocatalysis, spintronic materials, and AI-assisted materials discovery



Saeedeh Mohammadi

Dr. Esmail Doustkhah is an Assistant Professor of Chemistry at Istinye University, Türkiye, and Director of the Clean Energy Research Center. He received his PhD in Chemistry in 2017 and subsequently worked as a JSPS Fellow at the National Institute for Materials Science, Japan, and as a Co-fund TUBITAK-Marie Skłodowska-Curie–TÜBİTAK Fellow at Koç University. His research focuses on integrating computational and experimental approaches in materials science and catalysis, with particular interests in layered materials, functional nanoarchitectures, surface chemistry, photocatalysis, electrocatalysis, and advanced catalytic processes for green transition, hydrogen generation, CO_2 conversion, and environmental remediation.



Esmail Doustkhah

1- Introduction 2

2- Exchange-Correlation Functionals for Photo- and Electrocatalytic Modeling 4

2-1- Screened Hybrid Functionals for Accurate Electronic Bandgaps: HSE06 7

2-2- Many-Body Perturbation Theory: The *GW* Approximation 9

2-3- Semi-Local Meta-GGA Potential: The TB-mBJ Approach for Bandgap Prediction 10

3- Heterojunction Architectures and Interfacial Charge-Separation Mechanisms 12

3-1- Role of Magnetic Heterostructures in Photocatalytic Performance 13

3-2- Strain-Induced Modulation of Electronic Structure and Band Edges in Photocatalysts 19

4- Conclusion 23

5- Challenges and Future Perspectives 24

5-1- Accuracy of Exchange–Correlation Functionals and Electronic Structure Descriptions 24

5-2- Modeling Realistic Electrochemical and Photocatalytic Environments 24

5-3- Limitations of Thermodynamic Descriptors and Reaction Mechanisms 24

5-4- Complexity of Magnetic Heterostructures and Interfacial Charge Transfer 25

5-5- Predictive Limits of External Electric Fields and Strain Engineering 25

5-6- Stability, Selectivity, and Long-term Catalytic Performance 25

5-7- Computational Cost and Methodological Reproducibility 25

5-8- Bridging Computational Predictions and Experimental Validation 25

5-9- Future Directions 26

1- Introduction

Sustainable development has become a major focus of scientific research, driven in part by the environmental challenges associated with the extensive consumption of fossil fuels. Hydrogen (H_2) has emerged as a promising alternative energy carrier because of its high gravimetric energy density and carbon-free utilization. In this context, water electrolysis powered by electricity generated from renewable energy sources offers an environmentally sustainable approach to hydrogen production, with the potential to support the transition toward a low-carbon energy system [1–7].

The development of cost-effective, highly efficient, and durable electrocatalysts is essential for advancing water electrolysis, as these materials can reduce the overpotentials required to drive the hydrogen evolution reaction (HER) and oxygen evolution reaction (OER). Accordingly, considerable research efforts have been directed toward the design and optimization of electrocatalytic materials. Existing strategies include the discovery of novel compositions [8–11], morphological engineering [12], crystallinity control [13, 14], facet engineering [15], compositional modulation [16, 17], defect engineering [18-22], phase regulation [23], and the integration of different materials to exploit synergistic effects [24–27]. Despite these advances, the overall catalytic activity and operational stability of many non-noble-metal electrocatalysts remain inferior to those of noble-metal-based counterparts, highlighting the need for further advances in catalyst design.

To overcome these limitations, increasing attention has been directed toward strategies that extend beyond the intrinsic properties of electrocatalysts. Field-assisted electrocatalysis has emerged as a promising approach in which external physical stimuli are introduced to modulate electrochemical reactions, providing an additional means of controlling catalytic activity and reaction kinetics. Notably, improvements in the HER and OER have been reported through the application of various stimuli, including electric and magnetic fields, mechanical strain, and light irradiation. These approaches offer new opportunities to regulate interfacial charge transfer, modify the electronic structure of active sites, and facilitate reaction pathways, thereby enhancing overall electrocatalytic performance. Several studies have demonstrated the potential of field-assisted electrocatalysis to improve water-splitting performance. For instance, applying a back-gate voltage of 5 V substantially enhances the HER activity of MoS_2 nanosheets, reducing the overpotential required to achieve a current density of -100 mA cm^{-2} from 240 to 38 mV [28]. Similarly, the application of a moderate magnetic field ($\leq$ 450 mT) to an electrocatalytic anode composed of highly magnetic materials increases the current density during alkaline water electrolysis by more than 100% [29]. Mechanical strain also provides an effective means of tuning catalytic activity; the HER performance of β-PdH_x improves progressively as the applied strain increases from 0% to 4.5% [30]. In another example, infrared irradiation produces an approximately threefold increase in the HER current density of an Au–MoS_2 electrocatalyst [31]. Collectively, these findings highlight the potential of external-field-assisted strategies to enhance electrocatalytic activity beyond the limitations imposed by the intrinsic properties of conventional catalysts. Furthermore, such strategies offer several practical advantages, including operational simplicity and the possibility of dynamic, continuous, and reversible modulation of catalytic performance, with potential applicability across diverse electrocatalytic systems.

The OER is commonly described by the adsorbate evolution mechanism (AEM), which involves four consecutive proton-coupled electron-transfer steps at catalytic active sites. In this pathway, surface-bound intermediates are sequentially formed through the adsorption and deprotonation of oxygen-containing species, following the general sequence *OH → *O → *OOH → *O_2, ultimately leading to O_2 release [32]. A fundamental limitation of the AEM arises from the scaling relationship between the Gibbs free energies of the *OH and *OOH intermediates, expressed as $\Delta G(*OOH) = \Delta G(*OH) + 3.2$ eV [32]. This relationship reflects the interdependence of

intermediate binding energies and imposes constraints on the simultaneous optimization of the elementary reaction steps, thereby limiting the minimum achievable OER overpotential. To overcome this limitation and approach the apex of the OER activity volcano, various catalyst-engineering strategies have been explored, including heteroatom doping, vacancy engineering, and alloying, all of which aim to modify the electronic structure of active sites and optimize the adsorption energetics of reaction intermediates [33]. Nevertheless, the scaling relationship constrains the independent optimization of intermediate adsorption energies and does not fully account for the interactions among multiple reaction intermediates. Consequently, the conventional adsorbate evolution mechanism imposes a theoretical lower limit on the OER overpotential of approximately 0.37 V. Overcoming this limitation by breaking or circumventing the scaling relationship has therefore become an important research direction in electrocatalysis. Developing catalyst designs that enable independent regulation of intermediate binding energies could facilitate more favorable reaction energetics, reduce the intrinsic OER overpotential, and overcome the activity limitations associated with the conventional OER volcano relationship.

The lattice oxygen mechanism (LOM) has emerged as an alternative pathway for the oxygen evolution reaction that may overcome some of the limitations associated with the conventional AEM [34]. Unlike the AEM, the LOM involves the participation of lattice oxygen in O–O bond formation, potentially enabling direct coupling between oxygen species without requiring the formation of the conventional *OOH intermediate. By introducing an alternative reaction pathway, the LOM offers the possibility of circumventing the conventional scaling relationship between adsorbed intermediates and thereby improving OER kinetics. For example, Hou et al. [35] demonstrated that a transition from the AEM to the LOM can substantially enhance OER performance in layered bimetallic nitride/hydroxide materials. Similar lattice-oxygen-mediated pathways have also been reported during OER on FeCoCrNi alloy films [36], highlighting the potential of LOM-based catalyst design to improve electrocatalytic activity.

Although numerous studies have demonstrated that the LOM can circumvent conventional scaling relationships among reaction intermediates and potentially achieve lower theoretical overpotentials than the AEM, several critical challenges remain. First, the relatively high energy of the O 2p states near the Fermi level can facilitate electron depletion from lattice oxygen, promoting the formation of oxygen-centered holes and lattice oxygen oxidation. However, the electronic structure associated with these oxygen states may also hinder the deprotonation of adsorbed intermediates during the initial steps of the OER ($H_2O \rightarrow *OH \rightarrow *O$), thereby restricting further improvements in catalytic kinetics [37]. Second, the formation and migration of lattice oxygen vacancies under operating conditions can disrupt the local coordination environment of metal centers. These changes may promote metal-ion dissolution, structural reconstruction, and eventual degradation of the catalyst, compromising its long-term operational stability [38]. Addressing these kinetic and stability challenges is therefore essential for realizing the full potential of LOM-based electrocatalysts.

Two-dimensional (2D) layered materials have attracted considerable attention for electrocatalytic applications because of their large specific surface areas, favorable mechanical properties, and potentially high electrical and thermal conductivities [39]. In particular, two-dimensional ferromagnetic (FM) materials may offer additional opportunities for OER catalyst design by combining the structural advantages of 2D materials with the potential influence of spin polarization on reaction kinetics. These characteristics make 2D layered ferromagnets promising candidates for next-generation, high-performance OER electrocatalysts. However, the practical application of previously reported 2D FM materials has been hindered by two major limitations: Curie temperatures (T_C) below room temperature and insufficient stability under ambient atmospheric conditions [40]. Recent advances have nevertheless demonstrated the synthesis of a new class of air-stable, non-van der Waals ferromagnetic materials, namely, two-dimensional Cr_2X_3 compounds (X = S, Se, and Te). These developments open new possibilities for investigating the potential of robust 2D ferromagnets in electrocatalytic applications. But their T_C are not above room temperature as well. Therefore, how to realize room-temperature ferromagnetism in 2D Cr_2X_3 is the key issue to develop its applications in OER. Unfortunately, during catalytic processes, the reaction intermediate states and the corresponding electron transfer are difficult to capture. Therefore, the catalytic reaction mechanism is ambiguous, which hinders the further rational design of catalysts [39, 40].

To address these challenges, density functional theory (DFT) calculations, combined with chemical-probe experiments, have been employed to elucidate the possible coexistence and interplay of the AEM and the LOM during the OER [41]. In addition, the formation of heterostructures can introduce an internal electric field that modulates the electronic structure of the constituent materials. For example, a p–n heterojunction formed between $FeCo(OH)_2$ and Fe_2O_3 can induce a built-in electric field, thereby modifying interfacial charge distribution and regulating the catalytic properties of active sites. Such electronic modulation may facilitate the deprotonation of reaction intermediates while promoting lattice oxygen participation, potentially improving OER activity and catalyst stability simultaneously [41].

Over recent decades, DFT has evolved into an indispensable computational tool across a broad range of scientific disciplines, including physics, chemistry, materials science, biology, and medicine [42–44]. In catalysis research, the continuous development of advanced catalytic materials has increased the demand for detailed and reliable insights into reaction mechanisms at the atomic and electronic levels. Advances in computational methodologies, numerical accuracy, and computational resources have further expanded the capabilities of DFT, enabling the systematic investigation of complex catalytic systems and the evaluation of key parameters, such as electronic structure, adsorption energetics, and reaction pathways. Consequently, DFT calculations have become a powerful approach for elucidating catalytic mechanisms, identifying structure–activity relationships, and guiding the rational design of more efficient catalysts.

This review focuses on the application of DFT to electrochemical and photocatalytic processes, with particular emphasis on magnetic heterostructures, externally applied

electric fields, and strain engineering. First, the role of DFT in elucidating atomic and electronic structures and evaluating Gibbs free-energy changes (ΔG) in electrocatalytic reactions is discussed, highlighting its importance in understanding catalytic mechanisms and activity. Particular attention is also given to advanced electronic-structure methods, including the GW approximation, the Tran–Blaha modified Becke–Johnson (TB-mBJ) potential, and the Heyd–Scuseria–Ernzerhof (HSE06) hybrid functional, which can provide improved predictions of electronic band gaps relevant to electrochemical and photocatalytic applications. Second, the HER, oxygen reduction reaction (ORR), and electrochemical CO_2 reduction reaction (CO_2RR) are examined as representative case studies to demonstrate how DFT can elucidate reaction pathways, evaluate catalytic performance, and guide the rational design of efficient electrocatalysts. Rather than providing an exhaustive survey of the field, this review presents selected representative examples to establish a connection between DFT calculations and experimental investigations, thereby illustrating how theoretical insights can advance the understanding of electrocatalytic mechanisms and performance. Finally, the potential of DFT-guided approaches for the rational design of heterostructure-based electrocatalysts and photocatalysts is discussed. Key challenges and methodological limitations that must be addressed to improve the predictive accuracy and reliability of DFT-based catalyst design are also highlighted, along with future research directions toward the development of more efficient catalytic materials.

2- Exchange-Correlation Functionals for Photo- and Electrocatalytic Modeling

The DFT is a quantum-mechanical method widely employed to investigate the electronic structure and properties of many-electron systems, with extensive applications in heterogeneous catalysis and materials science. It provides a theoretical framework for evaluating catalyst properties and elucidating reaction mechanisms, including the thermodynamic and kinetic factors governing catalytic activity. The central principle of DFT is that the ground-state properties of an interacting many-electron system can be determined from its electron density, thereby avoiding the direct treatment of the more complex many-electron wave function. The theoretical foundation of DFT is established by the two Hohenberg–Kohn theorems, which demonstrate the fundamental relationship between the ground-state electron density and the external potential of the system [45,46]. The first Hohenberg–Kohn theorem establishes that the ground-state electron density uniquely determines the external potential and, consequently, the ground-state properties of an interacting many-electron system. The second theorem introduces a variational principle, according to which the ground-state energy corresponds to the minimum of the energy functional with respect to the electron density. In practical applications, DFT is commonly implemented through the Kohn–Sham formalism [47], which maps the interacting many-electron system onto an auxiliary system of noninteracting electrons subject to an effective potential. The resulting Kohn–Sham (KS) equations are solved self-consistently until the electron density and total energy satisfy the prescribed convergence criteria, enabling the systematic evaluation of the structural, electronic, and energetic properties of the system.

In heterogeneous catalysis, DFT enables the investigation of reaction energy profiles along different pathways on catalyst surfaces, facilitating the identification of energetically favorable intermediates and reaction products. Adsorption-energy calculations provide quantitative information on the binding strengths of reactants, intermediates, and products, helping to elucidate their roles in determining catalytic activity and selectivity. Furthermore, electronic-structure analyses, including the density of states (DOS) and electronic band structure, reveal the electronic characteristics of catalytic materials and support the identification of structure–activity relationships for rational catalyst design. DFT can also be employed to identify transition states and determine activation energies for elementary reaction steps. These calculations provide valuable insights into kinetic barriers and the relative feasibility of competing reaction pathways, complementing thermodynamic analyses in the mechanistic understanding of catalytic processes (Figure 1). DFT-based reaction pathway analysis enables the systematic evaluation of competing elementary steps, providing insights into the kinetic feasibility of catalytic processes. In addition, ab initio molecular dynamics (AIMD), which derives atomic forces from quantum-mechanical calculations rather than relying on classical force fields, can be used to investigate the time-dependent behavior of catalytic systems under finite-temperature conditions. This approach provides valuable information on reaction mechanisms, structural evolution, and thermal stability, while simulations performed under appropriate thermodynamic ensembles can help elucidate the influence of temperature and pressure on catalyst properties and performance.

The DFT has become an essential computational tool in photocatalysis and photoelectrocatalysis, providing fundamental insights into reaction mechanisms and material-design strategies [48]. By describing the electronic structure of catalytic materials at the quantum-mechanical level, DFT enables the evaluation of electronic energy levels, band structures, and related properties that govern their light-harvesting and catalytic behavior. These calculations help elucidate the underlying processes involved in photocatalysis and photoelectrocatalysis systems, including reactant adsorption, the formation and transformation of reaction intermediates, surface reaction steps, and product desorption. Such atomistic-level insights facilitate the identification of key factors controlling catalytic performance and support the rational design and optimization of materials for solar-driven chemical conversion. A detailed understanding of these processes are essential for elucidating the fundamental factors that govern photocatalytic and photoelectrocatalytic performance. Solar-driven water splitting, which converts water into hydrogen (H_2) using sunlight, represents a promising approach to sustainable hydrogen production. DFT calculations provide valuable insights into the electronic properties of catalytic materials, facilitate the identification of potential active sites, and enable the evaluation of reaction pathways, thereby supporting the rational design of more efficient photocatalysts and photoelectrocatalysts. Accordingly, computational investigations commonly examine band-edge positions, band alignment, and the effects of dopants and structural defects on charge-carrier behavior and

surface reaction energetics. These analyses help establish relationships between material composition, electronic structure, and catalytic performance, guiding the development of materials with improved efficiency for solar-driven hydrogen production.

Photocatalytic dye degradation is an important application of advanced oxidation processes for wastewater treatment and environmental remediation. DFT calculations can elucidate the interactions between photocatalyst surfaces and dye molecules by evaluating adsorption energies, examining plausible degradation pathways, and assessing how surface functionalization or structural modifications influence reaction energetics. In addition, the conversion of CO_2 into value-added chemical products, including hydrocarbons, through photocatalytic and photoelectrocatalytic processes offers a promising approach to carbon utilization and recycling. DFT provides a means of investigating CO_2 adsorption and activation, identifying reaction intermediates, and evaluating competing reaction pathways, thereby supporting the design of catalytic materials with improved activity and product selectivity for solar-driven CO_2 conversion. DFT calculations provide valuable insights into CO_2 activation on photocatalyst and photoelectrode surfaces, the energetics of reaction intermediates and elementary steps, and the optimization of catalytic materials to promote the formation of desired products. Similarly, photocatalytic and photoelectrocatalytic nitrogen reduction have attracted considerable attention as potential alternatives to the conventional Haber–Bosch process, offering prospects for more sustainable NH_3 synthesis.

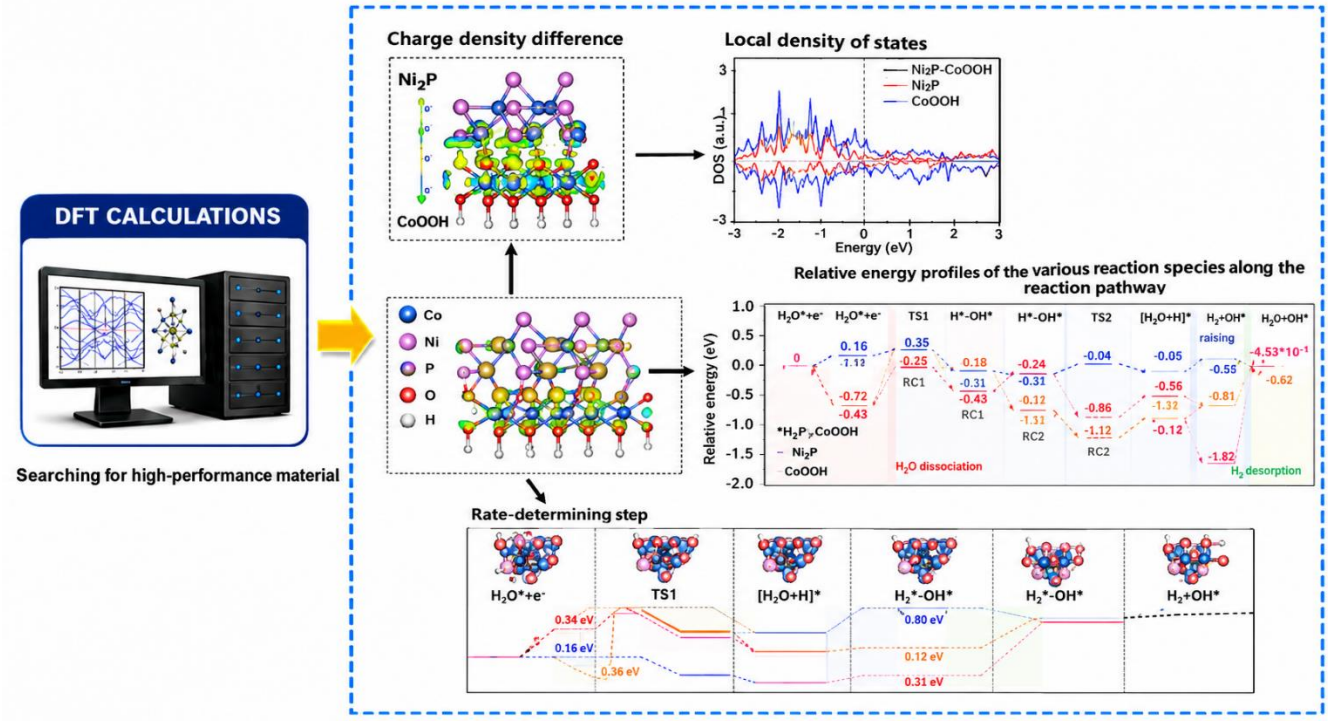


Figure 1. Representative DFT calculations and corresponding results for the Ni_2P–CoOH system, including charge-density difference, local density of states (LDOS), identification of the rate-determining step, and assessment of the relative thermodynamic feasibility of competing reaction pathways. These analyses provide complementary insights into the electronic structure, catalytic reaction mechanisms, and energetics of the underlying processes [49]. Adapted from Zhing et al. [50], with permission from *Nano-Micro Letters*, 12 (2020), 140. Copyright © 2020 Springer Nature.

DFT studies can elucidate the mechanisms of N_2 adsorption and activation, characterize successive hydrogenation steps, and assess how surface functionalization, structural modifications, and active-site properties affect reaction energetics and product selectivity. Across these applications, DFT has become a valuable tool not only for interpreting experimental observations and elucidating reaction mechanisms, but also for predicting promising materials and guiding the experimental design, synthesis, and evaluation of novel photocatalysts and photoelectrocatalysts. The integration of theoretical calculations with experimental investigations is therefore essential for developing more efficient and environmentally sustainable approaches to energy conversion and chemical production. From this perspective, this review highlights key advances in the application of DFT to mechanistic investigations of photocatalytic and photoelectrocatalytic systems, with particular emphasis on hydrogen production, dye degradation, CO_2 reduction, and N_2 reduction. We also examine the key challenges and future prospects associated with the application of DFT, aiming to provide researchers with a comprehensive perspective on improving its scope, reliability, and predictive accuracy in the modeling of photocatalysts and photoelectrocatalytic.

DFT calculations enable the investigation of electronic band structures and the estimation of bandgap energies, providing essential information about the electronic properties of photocatalytic materials. This approach is particularly useful for identifying new electronic states introduced by doping or heterojunction formation. Partial charge density analysis can further clarify the spatial distribution and localization of these states, helping to elucidate their roles in photocatalytic and photoelectrocatalytic processes. In addition, density of states and projected density of states (PDOS) analyses provide insights into the contributions and hybridization of atomic orbitals near the Fermi level. These analyses help characterize the electronic interactions and bonding characteristics among

constituent elements, thereby improving the understanding of structure–property relationships in photocatalysts and photoelectrodes. Furthermore, adsorption energy calculations are essential for quantifying the interaction strength between adsorbed species and catalyst surfaces, providing insight into the stability of adsorbed intermediates and the feasibility of subsequent reaction steps. Charge-transfer processes can be further investigated using charge density difference and Bader charge analyses. The charge density difference analysis reveals the spatial redistribution of electronic charge upon adsorption or interface formation, offering an initial picture of charge accumulation and depletion. Complementarily, Bader charge analysis provides a quantitative estimate of charge transfer between constituent atoms or interfacial components, helping clarify the role of electronic redistribution in catalytic activity. Bader charge analysis complements these investigations by quantifying the electron gain or loss of individual atoms, thereby providing further insight into interfacial charge redistribution. However, charge analysis alone does not establish the pathways of charge-carrier transport, which require additional evaluation of the electronic structure and interfacial properties. Furthermore, DFT calculations can be used to determine the work function of a material, providing valuable information about its surface electronic properties and facilitating the assessment of band alignment at interfaces. When combined with band-edge positions and interfacial electronic structure analysis, work-function calculations help clarify the driving forces governing charge separation and transfer in photocatalytic and photoelectrocatalytic systems. Work-function calculations are essential for predicting electronic interactions at heterojunction interfaces, which can strongly influence charge separation, interfacial charge transfer, and the overall performance of photocatalytic and photoelectrocatalytic systems. In addition, calculating Gibbs free-energy changes along reaction pathways provides a useful framework for evaluating reaction thermodynamics and identifying potentially rate-limiting steps. Comparing the free-energy changes associated with individual elementary steps helps clarify the energetic requirements of the overall reaction and identify the factors that govern catalytic efficiency. Together, these computational analyses provide a theoretical basis for rational materials design and the development of more efficient photocatalytic and photoelectrocatalytic systems.

High-throughput (HT) calculations are an essential component of computational materials screening and discovery. These approaches enable the systematic evaluation of material properties by performing large numbers of DFT simulations across extensive materials databases. Implementing HT workflows requires robust data-management strategies for collecting, storing, processing, and analyzing large datasets, as well as reliable systems for distributing, coordinating, and monitoring computational tasks. Dedicated workflow automation and resource-management tools are therefore necessary to ensure efficient and reproducible execution of HT-DFT calculations. To date, numerous HT screening frameworks have been developed, many of which provide application programming interfaces for integrating with various DFT simulation packages, including the Vienna Ab initio Simulation Package (VASP) [50], the Cambridge Serial Total Energy Package (CASTEP) [51], Quantum ESPRESSO (QE) [53], DMOL3 [53], ABINIT [54], and WIEN2k [55]. Figure 2 summarizes representative HT-DFT calculations packages.

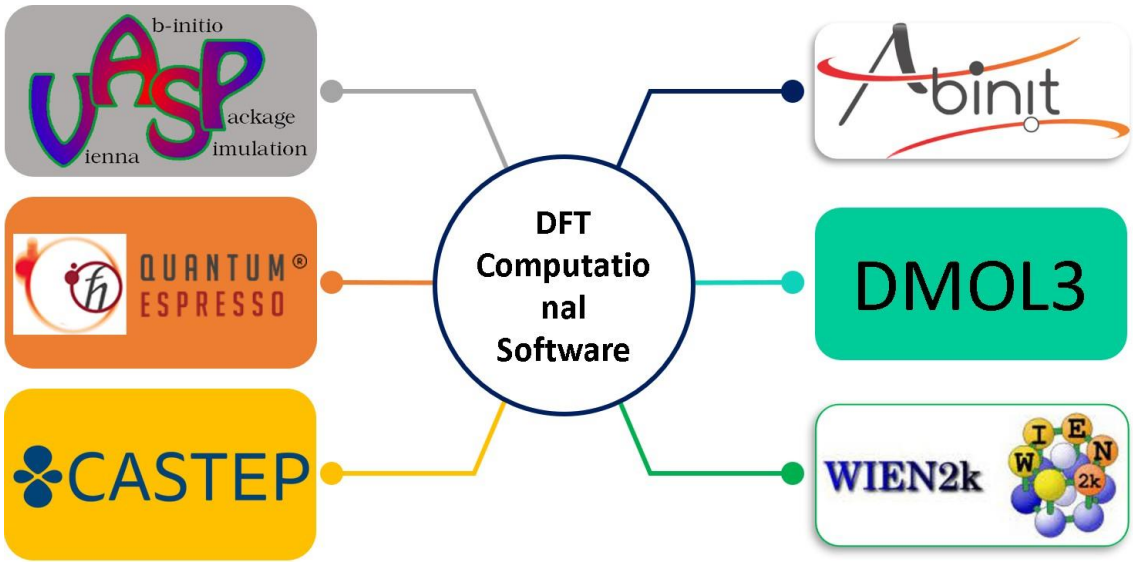


Figure 2. Overview of representative high-throughput density functional theory (HT-DFT) computational packages used for automated first-principles calculations and high-throughput materials screening.

In DFT, various approximations are employed to solve the KS equations numerically. The choice of approximation directly affects both the computational cost and the accuracy of the results, with the exchange–correlation functional playing a particularly important role. In principle, an exact exchange–correlation functional would yield the exact ground-state energy and electron density within the framework of DFT. However, the exact functional is not known, and practical calculations therefore rely on approximate forms. Among the most widely used are the local density approximation (LDA) and the generalized gradient approximation (GGA), which often provide satisfactory descriptions of ground-state structural and energetic properties. Nevertheless, these functionals generally underestimate bandgap energies and have limitations in describing excited-state properties [56, 57]. The problems, to some extent, can be overcome by choosing more expensive exchange-correlation functionals, Such as

Heyd–Scuseria–Ernzerhof (HSE) hybrid functional [58], modified Becke–Johnson potential (mBJ) [59,60].

These limitations can be partially addressed by employing more computationally demanding approaches, such as the HSE hybrid functional [58], the mBJ exchange potential [59,60]., and the *GW* approximation, which incorporates the Green's function (G) and the screened Coulomb interaction (W) [61]. These methods can provide improved descriptions of electronic band structures and bandgap energies, although their computational requirements and accuracy depend on the material system and the specific implementation (Figure 3).

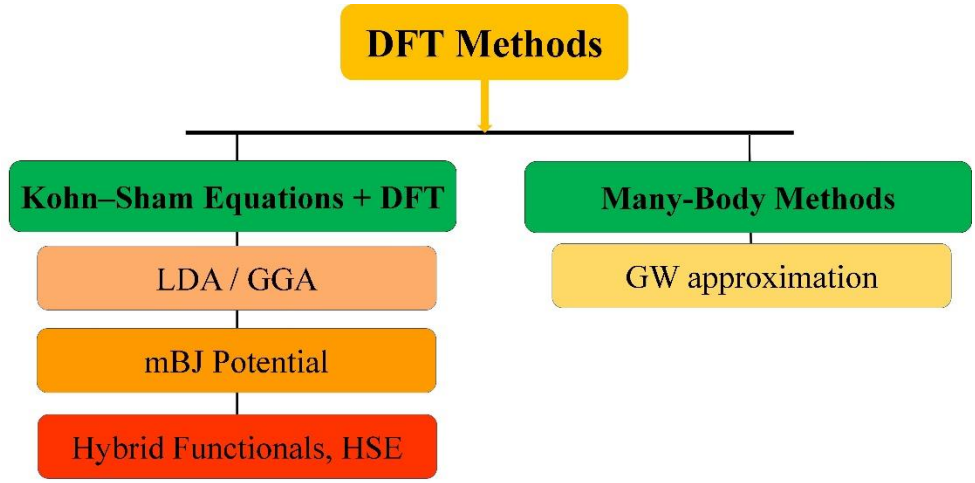


Figure 3. Classification of density functional theory (DFT) methods according to their underlying theoretical frameworks and levels of approximation, highlighting the hierarchical development of exchange–correlation functionals and advanced electronic-structure approaches.

2-1- Screened Hybrid Functionals for Accurate Electronic Bandgaps: HSE06

Hybrid density functionals incorporate a fraction of Hartree–Fock (HF) exchange into conventional exchange–correlation approximations, often improving the accuracy of electronic structure predictions compared with generalized gradient approximation (GGA) functionals. This improvement is partly attributed to the treatment of nonlocal exchange, which helps address certain limitations of semilocal functionals in describing electron localization and exchange interactions. Efficient implementations of hybrid functionals for periodic solids have been developed using Gaussian-type orbitals and periodic boundary conditions [62, 63]. In parallel, linear-scaling DFT and HF methods have been developed to reduce computational costs substantially, making calculations on large and complex systems more feasible [64-66].

The fast multipole method provides an efficient approach for evaluating long-range Coulomb interactions in extended systems [67-69]. However, its conventional formulation cannot be directly applied to HF exchange calculations because the exchange interaction involves a different contraction pattern between electron-repulsion integrals and the density matrix.

Kohn demonstrated that the spatial range of exchange interactions in insulating systems decays exponentially, with the decay rate related to the HOMO–LUMO gap or the bandgap in periodic materials [70]. In contrast, benchmark calculations indicate that exchange interactions in metallic systems exhibit algebraic decay. Several truncation schemes have been developed to exploit the rapid decay of exchange interactions in systems with sufficiently large bandgaps [71, 72]. However, these techniques offer limited computational savings for materials with small or vanishing bandgaps. Consequently, hybrid-functional calculations can be substantially more computationally demanding than conventional DFT calculations that do not include HF exchange [73].

In periodic boundary condition calculations, the HF exchange energy can be evaluated in real space by summing the contributions from significant interactions within the reference unit cell and between that cell and its neighboring cells. The contributions from individual cells can be analyzed as a function of their distance from the reference cell. As discussed above, these contributions decay slowly in metallic systems, making convergence with respect to the interaction range particularly challenging. Consequently, achieving full convergence of HF exchange calculations for metals can require substantial computational effort [73].

Heyd and Scuseria introduced a range-separated hybrid functional in which exact HF exchange is incorporated only into the short-range component of the exchange interaction, while the long-range contribution is described using DFT. This approach allows the exchange hole to extend over neighboring regions around a reference point while limiting the contribution of exact exchange at larger distances [73].

The PBE0 hybrid functional [74-78], developed from the Perdew–Burke–Ernzerhof (PBE) exchange–correlation functional introduced by Perdew et al.,[75] combines a fraction of exact HF exchange with the PBE exchange and correlation contributions. Its exchange–correlation energy is expressed as follows:

$$E_{XC}^{PBE0} = aE_X^{HF} + (1-a)E_X^{PBE} + E_C^{PBE}, \quad (1)$$

Here, the mixing parameter (a = 1/4) is derived from perturbation theory [74]. The following discussion focuses on the expression for the exchange energy.

$$E_X^{PBE0} = aE_X^{HF} + (1-a)E_X^{PBE} \quad (2)$$

Each term is then decomposed into its short-range and long-range contributions as follows [73]

$$E_X^{PBE0} = aE_X^{HF,SR}(\omega) + aE_X^{HF,LR}(\omega) + (1-a)E_X^{PBE,SR}(\omega) + E_X^{PBE,LR}(\omega) - aE_X^{PBE,LR}(\omega). \quad (3)$$

Numerical evaluations using physically relevant values of the screening parameter ω show that the long-range HF and PBE exchange contributions are relatively small, accounting for only a few percent of the total exchange energy, and largely cancel one another. Neglecting these contributions, under the assumption that the resulting approximation is compensated for by other terms in the functional, leads to a screened hybrid density functional based on the Coulomb potential, expressed as follows [73]

$$E_{XC}^{\omega PBEh} = aE_X^{HF,SR}(\omega) + (1-a)E_X^{PBE,SR}(\omega) + E_X^{PBE,LR}(\omega) + E_C^{PBE}, \quad (4)$$

Here, ω is an adjustable screening parameter that controls the range of the short-range exchange interaction. The ωPBE hybrid functional, commonly denoted as ωPBEh, recovers the PBE0 functional when ω = 0 and approaches the PBE functional in the limit ω → ∞. The following sections present the derivation of the short-range and long-range contributions appearing in Eq. (4).

The authors also compare the proposed ωPBEh functional with a PBE0-type hybrid functional in which the full-range HF exchange is replaced by its screened short-range component [73].

$$E_{XC}^{SR,HF\ PBE0} = aE_X^{HF,SR} + (1-a)E_X^{PBE} + E_C^{PBE}, \quad (5)$$

Here, the mixing coefficient is a = 1/4. The mean absolute errors (MAEs) in the standard enthalpies of formation at 298 K were evaluated as a function of the screening parameter ω, with the results for the G2-1 benchmark set comprising 55 small molecules[32] presented in Fig. 2. At ω = 0, the ωPBEh functional reproduces the PBE0 results, apart from minor differences arising from the parametrization of the PBE and ωPBE exchange holes. In the limit ω → ∞, the functional converges to the nonhybrid PBE approximation. Furthermore, increasing ω substantially reduces the computational cost associated with evaluating short-range HF exchange.

HSE06 hybrid-functional calculations have revealed half-metallic electronic characteristics in $CuCoO_2$, which may contribute to its potential multifunctionality in photocatalytic and electrocatalytic applications, as well as its multiple optical bandgaps [79]. In another study, Zhao et al. developed a machine-learning model to predict the types of two-dimensional van der Waals heterostructures (vdWHs) based on g-GaN by introducing a simplified energy-band-shift hypothesis. The proposed hypothesis was subsequently validated through first-principles calculations. To improve the accuracy of the predicted electronic bandgaps and obtain values closer to experimental measurements, the authors employed the HSE06. The results confirmed the validity of the proposed band-shift hypothesis for g-GaN-based vdWHs that do not contain elements from the first transition-metal series, with the classification model achieving an area under the receiver operating characteristic curve of 0.93. Furthermore, a regression model was developed to predict the bandgap values of type-II g-GaN-based vdWHs whose band-edge positions satisfy the requirements for photocatalytic water splitting. The model achieved a mean absolute error (MAE) of 0.24 eV (Figure 4). This study provides a machine-learning-based screening framework for identifying promising g-GaN-based vdWHs for photocatalytic applications, thereby substantially improving screening efficiency [80].

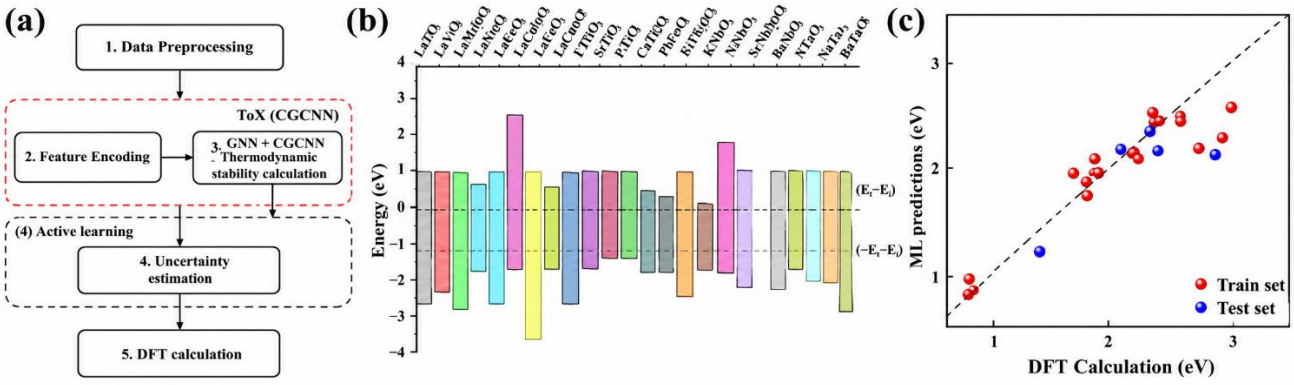


Figure 4. (a) Schematic illustration of the screening workflow for type-II van der Waals (vdW) heterostructures based on two-dimensional g-GaN, involving the initial selection of suitable partner materials followed by the evaluation of the resulting heterostructures. (b) Band-edge alignment of the g-GaN/X heterostructures relative to the vacuum level. (c) Machine-learning predictions obtained using a random forest regressor, comparing the predicted values for the training set (red circles) and test set (blue circles) with the corresponding HSE06-calculated results [80]. Adapted from Zhao et al. [80], with permission from *Applied Surface Science*, 640 (2023), 158400. Copyright © 2023 Elsevier.

2-2- Many-Body Perturbation Theory: The *GW* Approximation

The *GW* approximation provides an effective approach for estimating the electronic self-energy [81]. In this method, the exchange interaction is treated exactly, whereas electronic screening is described within the random-phase approximation (RPA), which accounts for the infinite-order summation of noninteracting electron-hole ring diagrams. *GW* calculations are widely employed to predict electronic excitation energies and quasiparticle lifetimes from first principles, complementing DFT, which is primarily designed to describe the electronic ground state.

The computational demands of hybrid-functional and *GW* calculations have led most implementations [82-84] to rely on pseudopotential-based plane-wave methods, which can limit the range of materials that can be investigated efficiently. These limitations are particularly relevant for systems containing transition metals, rare-earth elements, and oxygen. Early all-electron *GW* studies addressed this challenge using the linearized augmented plane-wave (LAPW) method. Hamada et al. [85] applied this approach to Si, while Aryasetiawan [86] investigated Ni. In subsequent developments, all-electron *GW* implementations were introduced using several computational approaches, including the full-potential LAPW (FLAPW) method [87,88], the linearized muffin-tin orbital (LMTO) method [89-91], the projector-augmented-wave (PAW) method [92-94], and the Korringa–Kohn–Rostoker (KKR) method [95]. These advances enabled *GW* calculations to be applied to a broader range of material systems. Although an early implementation of hybrid functionals employed a Gaussian-type basis set [96], their integration into all-electron computational frameworks was achieved only in more recent years. In 2005, Paier et al. [97] implemented hybrid functionals using the PAW method. The following year, Novak et al. [98] introduced an approximate implementation within the FLAPW framework, in which the nonlocal exchange contribution was evaluated only within individual atomic spheres and for selected angular-momentum channels. In 2010, Friedrich et al. [99] developed an efficient FLAPW-based implementation of hybrid functionals that overcame these restrictions. The FLAPW method offers a highly accurate all-electron basis suitable for investigating the electronic structures of a wide range of materials, including low-symmetry systems, open structures, transition-metal compounds containing d electrons, rare-earth systems involving f electrons, and oxides. A key advantage of this approach is that core and valence electrons are treated on an equal footing.

The *GW* approximation is a widely used approach for describing the electronic self-energy [82]. The self-energy accounts for the renormalization of an added electron or hole arising from its interactions with the surrounding electron system. By analyzing the renormalized Green's function, key properties of the many-electron system can be determined, including quasiparticle excitation energies and lifetimes. These quantities can be compared with experimental measurements, particularly those obtained from photoelectron spectroscopy.

The *GW* approximation treats the renormalization arising from electron exchange exactly while accounting for a substantial portion of the effects of electron correlation. In this framework, electronic screening is described within the RPA [100]. In a many-electron system, the bare Coulomb potential, $v(|r-r'|) = 1/|r-r'|$ generated by an electron at position r is screened by the redistribution of surrounding electrons. Within the RPA, this induced charge redistribution is described by the polarization function, initially neglecting the feedback of the induced charge on the potential. This feedback effect is subsequently incorporated by solving a Dyson-type equation [101]

$$P(r,r';\omega) = -i\sum_{\sigma}\lim_{\eta\to 0^+}\int_{-\infty}^{+\infty} d\omega' G^{\sigma}(r,r';\omega')G^{\sigma}(r,r';\omega'-\omega)e^{i\eta\omega'}, \quad (6)$$

where σ is the electron spin. Diagrammatically, P is represented by a bubble formed by two Green function lines. For the non-interacting G(r, r'; ω) we employ the KS Green function, which can be written in terms of the KS wave functions $\varphi^{\sigma}_{nk}(r)$ and energies $\varepsilon^{\sigma}_{nk}$ as $G^{\sigma}(r,r';\omega') = \sum_{nk}\varphi^{\sigma *}_{nk}(r')/\left[\omega-\varepsilon^{\sigma}_{nk}+i\eta\,\mathrm{sgn}(\varepsilon^{\sigma}_{nk}-\varepsilon_F)\right]$ with the Fermi energy ε_F, where **k** and n are the are the Bloch vector and the band index, respectively. Inserting into Eq. (6) yields [100]

$$P(r,r';\omega) = \lim_{\eta\to 0^+}\sum_{\sigma}\sum_{q,k}^{BZ}\sum_{n}^{occ}\sum_{n'}^{unocc}\varphi^{\sigma *}_{nq}(r)\varphi^{\sigma}_{n'k}(r)\varphi^{\sigma}_{nq}(r')\varphi^{\sigma *}_{n'k}(r') \times\left(\frac{1}{\omega+\varepsilon^{\sigma}_{nq}-\varepsilon^{\sigma}_{n'k}+i\eta}-\frac{1}{\omega-\varepsilon^{\sigma}_{nq}+\varepsilon^{\sigma}_{n'k}-i\eta}\right). \quad (7)$$

With the polarization function we obtain the dynamically screened interaction W(r, r'; ω) from the integral equation

$$W(r,r';\omega) = v(|r-r'|) + \int v(|r-r''|)P(r'',r''';\omega)W(r''',r';\omega)d^3r''d^3r''', \quad (8)$$

where the implicit infinite summation of this Dyson-type equation includes the feed-back effects mentioned above.

An expansion of the electronic self-energy $\Sigma^{\sigma}_{XC}(r,r';\omega)$ in terms of W up to linear order yields the *GW* approximation [101]

$$\Sigma_{\mathrm{XC}}^{\sigma}(\mathrm{r},\mathrm{r}';\omega)=\frac{\mathrm{i}}{2\pi}\lim_{\eta\to 0^{+}}\int \mathrm{G}^{\sigma}(\mathrm{r},\mathrm{r}';\omega+\omega')\,\mathrm{W}(\mathrm{r},\mathrm{r}';\omega')\,\mathrm{e}^{\mathrm{i}\eta\omega'}\mathrm{d}\omega'. \tag{9}$$

If we write the screened interaction as a sum of the bare interaction and a remainder,

$$\mathrm{W}(\mathrm{r},\mathrm{r}';\omega)=\mathrm{v}(|\mathrm{r}-\mathrm{r}'|)+\mathrm{W}^{\mathrm{c}}(\mathrm{r},\mathrm{r}';\omega), \tag{10}$$

the self-energy [Eq. (4)] decomposes into the terms

$$\Sigma_{\mathrm{X}}^{\sigma}(\mathrm{r},\mathrm{r}')=\frac{\mathrm{i}}{2\pi}\lim_{\eta\to 0^{+}}\int \mathrm{G}^{\sigma}(\mathrm{r},\mathrm{r}';\omega+\omega')\,\mathrm{v}(|\mathrm{r}-\mathrm{r}'|)\,\mathrm{e}^{\mathrm{i}\eta\omega'}\mathrm{d}\omega' \tag{11}$$

and

$$\Sigma_{\mathrm{c}}^{\sigma}(\mathrm{r},\mathrm{r}';\omega)=\frac{\mathrm{i}}{2\pi}\int \mathrm{G}^{\sigma}(\mathrm{r},\mathrm{r}';\omega+\omega')\,\mathrm{W}^{\mathrm{c}}(\mathrm{r},\mathrm{r}';\omega')\mathrm{d}\omega', \tag{12}$$

which are identified as the exchange and the correlation contributions to the electronic self-energy, respectively. We note that the exponential factor allows to close the integration path over the upper complex half plane in Eq. (11). As $\mathrm{W}^{\mathrm{c}}(\mathrm{r},\mathrm{r}';\omega')$ falls off quickly enough with increasing frequencies, we may take the limit $\eta \to 0$ before integrating in Eq. (12).

The excitation energies $\mathrm{E}_{\mathrm{nq}}^{\sigma}$ of the $N+1$ and $N-1$ particle system (for unoccupied and occupied states n, respectively) form the poles of the renormalized Green function, which can be calculated as corrections on the KS energies within first-order perturbation theory, yielding the nonlinear equation [101]

$$\mathrm{E}_{\mathrm{nq}}^{\sigma}=\varepsilon_{\mathrm{nq}}^{\sigma}+\left\langle\varphi_{\mathrm{nq}}^{\sigma}\middle|\Sigma_{\mathrm{XC}}^{\sigma}(\mathrm{E}_{\mathrm{nq}}^{\sigma})-\mathrm{v}_{\mathrm{XC}}^{\sigma}\middle|\varphi_{\mathrm{nq}}^{\sigma}\right\rangle, \tag{13}$$

Where $\mathrm{v}_{\mathrm{XC}}^{\sigma}(\mathrm{r})$ is the LDA exchange-correlation potential. While the expectation value of the latter and the KS energies are routinely calculated in the DFT code, we are left with the task of evaluating the expectation value $\left\langle\varphi_{\mathrm{nq}}^{\sigma}\middle|\Sigma_{\mathrm{XC}}^{\sigma}(\mathrm{E}_{\mathrm{nq}}^{\sigma})\middle|\varphi_{\mathrm{nq}}^{\sigma}\right\rangle$, which decomposes into an exchange and a correlation term according to Eqs. (6) and (7). Finally, we must solve the nonlinear Eq. (8). Because of the exponential factor in Eq. (6), we can formally close the frequency integration contour with an infinite half circle over the positive complex plane without changing the value of the integral. This contour integral then equals the sum over the residues of the poles of the Green function. The expectation value of the exchange term with respect to a wave function $\varphi_{\mathrm{nq}}^{\sigma}(\mathrm{r})$ yields the well-known HF expression [101]

$$\left\langle\varphi_{\mathrm{nq}}^{\sigma}\middle|\Sigma_{\mathrm{X}}^{\sigma}\middle|\varphi_{\mathrm{nq}}^{\sigma}\right\rangle=-\sum_{\mathrm{k}}^{\mathrm{BZ}}\sum_{\mathrm{n}'}^{\mathrm{occ.}}\int \varphi_{\mathrm{nq}}^{\sigma*}(\mathrm{r})\,\varphi_{\mathrm{n}'\mathrm{k}}^{\sigma}(\mathrm{r})\,\mathrm{v}(|\mathrm{r}-\mathrm{r}'|)\,\varphi_{\mathrm{n}'\mathrm{k}}^{\sigma*}(\mathrm{r}')\varphi_{\mathrm{nq}}^{\sigma}(\mathrm{r}')\,\mathrm{d}^{3}\mathrm{r}\,\mathrm{d}^{3}\mathrm{r}' \tag{14}$$

and from (14) we obtain

$$\left\langle\varphi_{\mathrm{nq}}^{\sigma}\middle|\Sigma_{\mathrm{c}}^{\sigma}(\omega)\middle|\varphi_{\mathrm{nq}}^{\sigma}\right\rangle=\frac{\mathrm{i}}{2\pi}\lim_{\eta\to 0^{+}}\sum_{\mathrm{k}}^{\mathrm{BZ}}\sum_{\mathrm{n}'}^{\mathrm{all}}\int_{-\infty}^{\infty}\mathrm{d}\omega' \times\int\frac{\varphi_{\mathrm{nq}}^{\sigma*}(\mathrm{r})\,\varphi_{\mathrm{n}'\mathrm{k}}^{\sigma}(\mathrm{r})\,\mathrm{W}^{\mathrm{c}}(\mathrm{r},\mathrm{r}';\omega')\,\varphi_{\mathrm{n}'\mathrm{k}}^{\sigma*}(\mathrm{r}')\,\varphi_{\mathrm{nq}}^{\sigma}(\mathrm{r}')}{\omega+\omega'-\varepsilon_{\mathrm{n}'\mathrm{k}}^{\sigma}+\mathrm{i}\eta\,\mathrm{sgn}(\varepsilon_{\mathrm{n}'\mathrm{k}}^{\sigma}-\varepsilon_{\mathrm{F}})}\mathrm{d}^{3}\mathrm{r}\,\mathrm{d}^{3}\mathrm{r}'. \tag{15}$$

In contrast to Eq. (15), the frequency integral in the latter expression cannot be replaced by a sum over residues because the poles of W^{c} are unknown.

2-3- Semi-Local Meta-GGA Potential: The TB-mBJ Approach for Bandgap Prediction

In general, when an orbital-independent potential is used, the bandgap obtained from the eigenvalue spectrum may differ from the fundamental bandgap, defined as the difference between the ionization potential I and the electron affinity A. This discrepancy arises from the derivative discontinuity of the exchange-correlation potential, Δ_{xc} [102, 103]. More accurate bandgap predictions can be achieved using alternative exchange-correlation functionals or computational methods. Applying the optimized effective potential (OEP) method to the exact-exchange functional can improve bandgap estimates; however, substantial underestimation or overestimation may still occur in certain cases [104,105]. Furthermore, several studies suggest that the improved bandgap predictions obtained using the OEP method may be partly coincidental. When exact exchange is combined with accurate *ab initio* correlation treatments within the OEP framework, the resulting bandgaps can be comparable to those predicted by the LDA. This behavior can be attributed, in part, to the significant contribution of the exchange-correlation derivative discontinuity, Δ_{xc} [106]. Hybrid functionals [107] are applicable to a broad range of solid-state materials, but their computational cost is considerably higher than that of semilocal functionals, although screened hybrid approaches can reduce this burden. The LDA+U method [108] has a computational cost comparable to that of semilocal functionals, but its applicability is largely limited to systems with localized electrons, such as those in 3d and 4f orbitals, and it requires

material-dependent parameters. The LDA combined with dynamical mean-field theory (LDA+DMFT) has also demonstrated considerable success [109], although it is computationally more demanding. The *GW* approximation can provide highly accurate bandgap predictions [110–112]; however, its computational requirements are substantial, particularly when self-consistency is included [112].

Tran and Blaha [113] investigated the Becke–Johnson (BJ) exchange potential proposed by Becke and Johnson [114], which was developed to reproduce the characteristic form of the exact-exchange OEP for atoms. Their results demonstrated that the BJ potential provides a more accurate description of bandgaps than the LDA and the PBE potential, a widely used GGA for solids [113, 115]. However, when combined with LDA correlation [116], the original BJ potential still substantially underestimates bandgaps, highlighting the need for further refinement. To address this limitation, Tran and Blaha introduced a straightforward modification of the BJ exchange potential that achieves bandgap accuracy comparable to that of computationally much more demanding methods.

Figure 6 compares the fundamental bandgaps of 23 solids calculated using the LDA and modified Becke–Johnson (mBJ-LDA) potentials. Tran and Blaha performed these calculations using the WIEN2k package, which implements the full-potential (linearized) augmented plane-wave plus local orbitals method [FP-(L)APW+lo] [117]. For comparison, the figure also presents experimental bandgap values, results obtained using the HSE03 and HSE06 hybrid functionals, and GW calculations. The *GW* data include all-electron non-self-consistent G_0W_0 results and fully self-consistent *GW* results. The present calculations, along with most theoretical results reported in the literature, were performed using experimentally determined crystal structures. The investigated materials encompass not only conventional sp semiconductors but also rare-gas solids, ranging from Ne to Xe, with bandgaps reaching approximately 22 eV, as well as the antiferromagnetic oxides MnO, FeO, and NiO, which exhibit strong correlations among their 3d electrons. For most of these materials, the mBJ-LDA potential yields bandgaps in good agreement with experimental measurements, typically with relative errors below 10%. For example, the calculated bandgaps of Ge and ScN are 0.85 and 0.90 eV, respectively, closely matching the experimental values of 0.74 and 0.90 eV. Similarly, good agreement is obtained for the medium-bandgap semiconductors SiC, ZnS, CdS, and AlP, with absolute errors below 0.25 eV. The method also performs well for wide-bandgap materials, including rare-gas solids, LiF, and LiCl. Among the 23 investigated solids, only MnO, FeO, and ZnO exhibit relative bandgap errors exceeding 15%. It is worth noting, however, that FeO is predicted to be metallic by the LDA (see Figure 5) [118].

Tran and Blaha demonstrated that highly accurate bandgaps for semiconductors and insulators can be obtained using an orbital-independent exchange-correlation potential constructed solely from semilocal quantities. Their approach represents a significant advance, as it achieves an accuracy comparable to that of computationally demanding hybrid-functional and *GW* methods while retaining the efficiency of semilocal approximations. Because band-structure calculations using this potential have a computational cost similar to that of the LDA and GGA, the method is well suited to the efficient investigation of large and complex material systems that would be considerably more expensive to treat using hybrid-functional or *GW* approaches.

O'Sullivan et al. employed DFT to investigate the structural stability and optoelectronic properties of phase-separated monolayer h-BCN structures, examining the effects of carbon concentration and domain size. To improve the accuracy of the electronic-structure predictions relative to the BP86-D3 approach [37,38], the authors evaluated several exchange-correlation functionals, including the revised Tao–Perdew–Staroverov–Scuseria (revTPSS) functional [39,40], the Tran–Blaha modified Becke–Johnson (TB-mBJ) potential [41,42], and the HSE06 [43,44]. For the HSE06 calculations performed using the Amsterdam Modeling Suite (AMS), the range-separation parameter, ω, was set to 0.11.

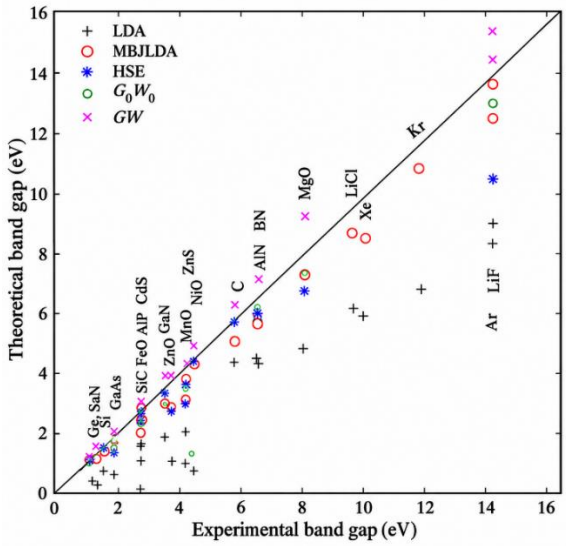


Figure 5. Comparison of theoretically predicted and experimentally measured bandgaps, illustrating the accuracy of the Tran–Blaha modified Becke–Johnson (TB-mBJ) potential in electronic-structure calculations. Reproduced from Tran and Blaha [118], *Physical Review Letters*, 102, 226401 (2009), with permission from the American Physical Society. Copyright © 2009 American Physical Society.

The authors found that increasing the carbon content reduces the energetic cost of carbon incorporation per atom, as the formation of a more graphitized network lowers the overall structural energy. HSE06 calculations further demonstrated that substantial carbon substitution within the domains of h-BN can reduce its bandgap from 5.94 to 1.61 eV at a carbon concentration of approximately 44 at.% (Table 1).

Table 1. HOMO and LUMO energy levels of the investigated h-BCN systems, corresponding electrochemical potentials relative to the normal hydrogen electrode (NHE), and voltage offsets with respect to the relevant oxidation and reduction potentials [118]. Reproduced from Tran and Blaha [118], *Physical Review Letters*, 102, 226401 (2009), with permission from the American Physical Society. Copyright © 2009 American Physical Society.

System	HOMO (eV)	V vs NHE (V)	Oxidation Offset (V)	LUMO (eV)	V vs NHE (V)	H_2 Reduction Offset (V)	CO_2 Reduction Offset (V)
BN	−7.23	2.79	1.56	−1.30	−3.14	−3.14	−2.90
BN-C_2	−6.60	2.16	0.93	−1.91	−2.53	−2.53	−2.29
BN-C_6	−6.66	2.22	0.99	−2.00	−2.44	−2.44	−2.20
BN-C_{24}	−5.96	1.52	0.29	−2.94	−1.50	−1.50	−1.26
BN-C_{54}	−5.58	1.14	−0.09	−3.42	−1.02	−1.02	−0.78

BN-C_{96}	−5.39	0.95	−0.28	−3.78	−0.66	−0.66	−0.42
Gr	−5.59	1.15	−0.08	−4.64	+0.20	+0.20	+0.44

These findings provide further evidence that phase-separated h-BCN structures offer considerable flexibility for tailoring electronic properties through compositional control. The catalytic potential of these materials was evaluated by comparing their conduction-band and valence-band edge positions with the redox potentials of the HER, OER, and CO_2 reduction reaction. This analysis identified three structures with suitable band-edge alignments for the considered catalytic processes. Their photoactivity was subsequently investigated using time-dependent density functional theory (TD-DFT), leading to the identification of two promising candidates for photocatalytic applications among the phase-segregated h-BCN structures.

3- Heterojunction Architectures and Interfacial Charge-Separation Mechanisms

Charge-carrier dynamics in semiconductor–semiconductor heterojunctions are governed by the formation of an interfacial space-charge region resulting from charge redistribution between the two materials [119, 120]. The resulting separation of charge carriers establishes an internal electric field that drives electrons and holes in opposite directions [121]. This process promotes charge-carrier separation, with electrons accumulating in the conduction band (CB) of the semiconductor with the more favorable reduction potential, while holes migrate to the valence band (VB) of the semiconductor with the more favorable oxidation potential [122]. Consequently, charge-carrier dynamics in heterojunctions promote more efficient electron–hole separation, facilitate interfacial charge transfer, and suppress charge-carrier recombination. These effects extend the lifetime of photogenerated charge carriers and ultimately enhance photocatalytic performance.

Conventional heterojunctions are generally classified into four main types: type-I, type-II, type-III, and direct Z-scheme heterojunctions, according to the relative alignment of their CB and VB edges [123,124]. In a type-I heterojunction, the CB edge of semiconductor A lies at a higher energy, while its VB edge lies at a lower energy, than the corresponding band edges of semiconductor B. Consequently, photogenerated electrons and holes accumulate in the CB and VB of semiconductor B, respectively, as illustrated in Figure 6(a) [125]. Because both charge carriers accumulate in the same semiconductor, their spatial separation is limited, which can facilitate rapid electron–hole recombination and reduce the overall efficiency of charge separation [125].

In type-II heterojunctions, the CB and VB edges of semiconductor A are both positioned at higher energies than the corresponding band edges of semiconductor B, as illustrated in Figure 6(b) [126]. This staggered band alignment promotes the migration and accumulation of photogenerated electrons in the CB of semiconductor B, while holes accumulate in the VB of semiconductor A, thereby facilitating spatial charge separation and suppressing electron–hole recombination [127]. In contrast, type-III heterojunctions exhibit a broken-gap band alignment in which the CB and VB edges of the two semiconductors are energetically separated without the conventional band overlap required for efficient interfacial charge transfer. This arrangement limits their ability to facilitate the spatial separation of photogenerated electron–hole pairs through conventional band-to-band transfer mechanisms, as shown in Figure 6(c) [128]. Type-II heterojunctions are therefore widely investigated for photocatalytic applications because their staggered band alignment facilitates charge separation and enables the regulation of charge-transfer pathways during catalytic reactions. However, type-II heterojunctions have a major thermodynamic limitation in photocatalytic applications: the enhanced charge-separation efficiency does not necessarily compensate for the reduced redox capability of the resulting charge carriers [129]. Specifically, photogenerated electrons accumulate in the CB of the semiconductor with a weaker reduction potential, while holes accumulate in the VB of the semiconductor with a weaker oxidation potential [130]. Consequently, despite suppressing electron–hole recombination, type-II heterojunctions may exhibit insufficient redox potentials to drive certain photocatalytic reactions efficiently. This charge-separation mechanism can limit the participation of photogenerated charge carriers in surface catalytic reactions. Furthermore, electrostatic interactions between oppositely charged carriers can influence interfacial charge transfer between the two semiconductors in type-II heterojunctions [131]. Consequently, the practical realization of the proposed charge-transfer mechanism may be hindered by limitations in interfacial charge transport and charge-carrier migration. In addition, the transfer of electrons and holes to semiconductor band edges with weaker reduction and oxidation potentials, respectively, reduces the overall redox capability of type-II heterojunctions, potentially limiting their photocatalytic performance.

Direct Z-scheme heterojunctions exhibit a band alignment similar to that of type-II heterojunctions, but the direction of interfacial charge transfer differs, as illustrated in Figure 6(d) [132]. The term S-scheme heterojunction is also used to describe a related charge-transfer mechanism [133]. Although both configurations involve staggered band alignment, the charge-transfer pathway in a direct Z-scheme heterojunction differs fundamentally from that in a conventional type-II heterojunction [132,134] In this mechanism, photogenerated electrons in the conduction band of semiconductor B, which possesses a strong reduction capability, and photogenerated holes in the valence band of semiconductor A, which exhibits a strong oxidation capability, are retained to participate in photocatalytic reactions [132]. When the two semiconductors come into close contact, electrons initially diffuse from semiconductor B to semiconductor A because of the difference in their Fermi levels, leading to interfacial charge redistribution and the establishment of an internal electric field [135]. This interfacial charge redistribution results in the formation of a depletion region on the side of semiconductor B and an electron-accumulation region on the side of semiconductor A, leaving semiconductor B positively charged and semiconductor A negatively charged. The resulting internal electric field promotes the recombination of photogenerated electrons in the CB of semiconductor A with holes in the VB of semiconductor B. This charge-transfer pathway is opposite to that typically proposed for type-II heterojunctions, allowing

electrons with strong reduction capability and holes with strong oxidation capability to remain available for photocatalytic reactions. Furthermore, intimate contact between the two semiconductors drives their Fermi levels toward equilibrium, resulting in interfacial band bending [135]. Band bending further facilitates interfacial electron transfer from the CB of semiconductor A to the VB of semiconductor B [136] The combined effects of the internal electric field, band bending, and electrostatic interactions promote the recombination of photogenerated electrons in the CB of semiconductor A, which have a relatively weak reduction potential, with holes in the VB of semiconductor B, which have a relatively weak oxidation potential [137]. This selective recombination eliminates charge carriers with weaker redox capabilities while preserving the highly reducing electrons in the CB of semiconductor B and the highly oxidizing holes in the VB of semiconductor A [138]. Consequently, Z-scheme heterojunctions enhance the effective spatial separation of the remaining photogenerated charge carriers while retaining their strong redox potentials, thereby improving their potential for photocatalytic applications [139].

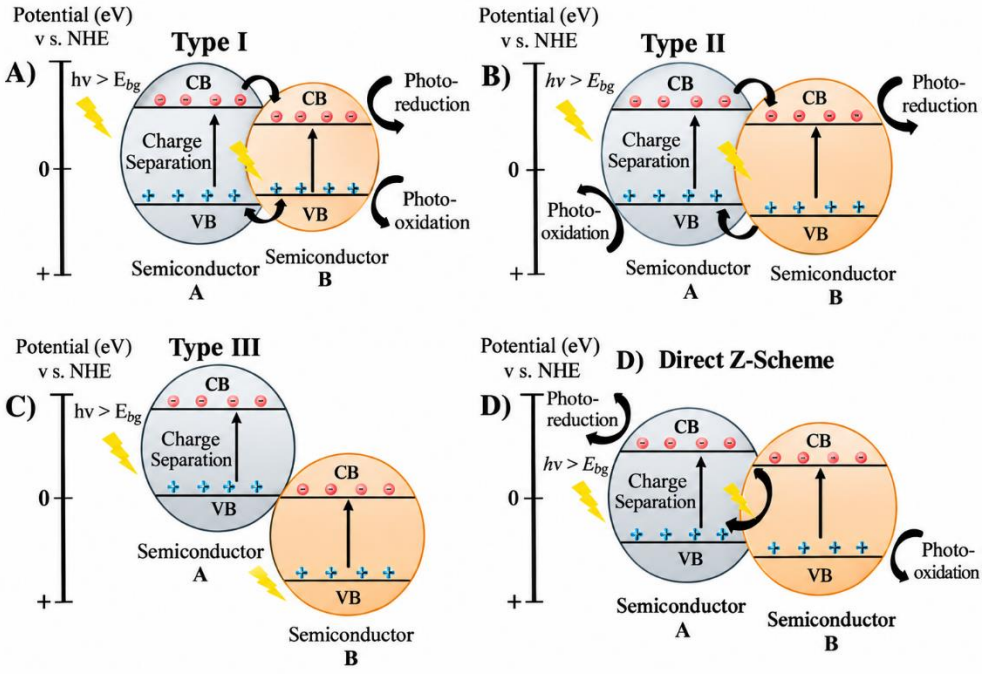


Figure 6. Schematic representations of different heterojunction configurations: (a) type-I, (b) type-II, (c) type-III, and (d) direct Z-scheme heterojunctions. Reproduced from Kumari et al. [119], *Materials Advances*, 3, 2309 (2022), with permission from the Royal Society of Chemistry. Copyright © 2022 Royal Society of Chemistry.

3-1- Role of Magnetic Heterostructures in Photocatalytic Performance

Compared with conventional strategies for enhancing photocatalytic performance, applying an external magnetic field during photocatalytic reactions offers a potentially efficient, safe, convenient, and contactless approach to improving photocatalytic activity. The underlying mechanisms involve magnetic interactions and spin-dependent processes, including spin–orbit coupling. Electrons possess intrinsic spin angular momentum and an associated magnetic moment, which gives rise to their magnetic response. When a photocatalyst is exposed to an external magnetic field, the field can influence the spin states and spin-dependent behavior of charge carriers, depending on its strength and orientation. These effects can modify charge-carrier dynamics and recombination pathways, potentially improving photocatalytic performance [140,141]. Spin–orbit coupling links the spin angular momentum of electrons to their orbital motion, whereas the interaction between an external magnetic field and the electronic magnetic moments can modify the energies of different spin states. This interaction lifts the degeneracy of the spin states, resulting in energy-level splitting known as the Zeeman effect. In a magnetic field, the spin states are commonly distinguished as parallel and antiparallel to the field direction, with their relative energies depending on the sign and magnitude of the electron's magnetic moment and the field strength. Consequently, the populations of the spin states may become unequal, producing spin polarization that can influence charge-carrier dynamics and photocatalytic processes [142].

Additionally, an external magnetic field can influence photogenerated charge carriers through the Lorentz force, which acts on moving charged particles in a magnetic field and can modify their trajectories and transport behavior. Under suitable conditions, these effects may promote electron–hole separation and influence charge-carrier recombination, thereby improving photocatalytic performance, particularly in magnetically responsive materials. Furthermore, magnetic-field-induced forces and particle motion may affect catalyst dispersion and agglomeration, potentially increasing the exposure of catalytically active sites and facilitating surface reactions [143].

Xin et al. (2023) [38] developed a Fe-Co(OH)$_2$/Fe$_2$O$_3$ heterostructure to enhance the OER by combining the adsorbate evolution mechanism (AEM) with the lattice oxygen mechanism (LOM). Their combined theoretical and experimental investigations revealed that Fe-Co(OH)$_2$ facilitates the deprotonation of OER intermediates, whereas Fe$_2$O$_3$ promotes O–O bond formation through the participation of lattice oxygen. To investigate the underlying catalytic mechanisms, DFT calculations were first performed to

examine the conventional four-step proton-coupled electron transfer pathway proposed by Nørskov et al. for the AEM (Figure 7(a)). The results indicated that pristine $Co(OH)_2$ exhibits an overpotential of 0.78 V, with the formation of *OOH identified as the potential-determining step (PDS), owing to the strong Co–O interaction (Figure 7(b)). Replacing one Co atom with Fe improved the adsorption energetics of the OER intermediates, reducing the calculated overpotential to 0.55 V at the Co site and 0.63 V at the Fe site. However, further Fe incorporation yielded only marginal improvements in catalytic activity because of intrinsic scaling relationships between the adsorption energies of OER intermediates and a shift in the PDS toward *O adsorption. These limitations constrain the catalytic performance attainable through the AEM alone (Figure 7(c)). In contrast, the electronic structure of Fe_2O_3 indicated the potential for an alternative reaction pathway involving lattice oxygen. Analysis of the PDOS revealed unoccupied metal–oxygen states near the Fermi level, with Fe_2O_3 exhibiting a higher density of unoccupied oxygen states above the Fermi level (E_F) (Figures 7(d) and 7(e)). These oxygen nonbonding states provide an electronic basis for lattice oxygen participation, supporting the feasibility of the LOM. However, the relatively weak *O adsorption on Fe_2O_3 makes the conversion of *OH to *O the potential-determining step (PDS), while the sluggish kinetics of subsequent protonation further limit its OER activity (Figure 7(c)). To address these complementary limitations, the Fe-$Co(OH)_2/Fe_2O_3$ interface was engineered to integrate the favorable reaction steps of both mechanisms. The resulting interfacial built-in electric field drives charge redistribution and modulates the electronic structures of both components (Figure 7(f)). Electron transfer from Fe_2O_3 reduces the population of unoccupied oxygen nonbonding states, thereby moderating lattice oxygen activation and oxygen-vacancy formation. This electronic modulation helps preserve the structural stability of Fe_2O_3 during the OER (Figure 7(d)). Concurrently, electron enrichment shifts the Co 3d states in Fe-$Co(OH)_2$ toward lower energies, lowering the d-band center and weakening the adsorption of *OH and *O intermediates, thereby facilitating subsequent reaction steps (Figure 7(e)). This interfacial electronic coupling allows Fe-$Co(OH)_2$ to promote deprotonation, while Fe_2O_3 facilitates O–O bond formation, reducing the accumulation of *OOH intermediates (Figure 7(g)). As a result, integrating the AEM and LOM pathways reduces the calculated OER overpotential to 0.34 V (Figure (i)).

In addition to enhancing catalytic activity, the heterostructure exhibits improved structural stability. Integrated crystal orbital Hamilton population (ICOHP) analysis indicates that the Co–O bonding characteristics are better preserved in the heterostructure than in pristine $Co(OH)_2$ during *O adsorption. Specifically, the reported ICOHP value for Co–O in pristine $Co(OH)_2$ decreases from 1.12 to 1.08 upon *O adsorption, whereas stronger Co–O bonding is maintained in the heterostructure (Figure 8h). These findings demonstrate how interfacial charge redistribution can regulate the adsorption of reaction intermediates, promote complementary OER pathways, and mitigate structural destabilization. Thus, the Fe-$Co(OH)_2/Fe_2O_3$ heterostructure represents a promising strategy for developing efficient and durable oxygen evolution electrocatalysts.

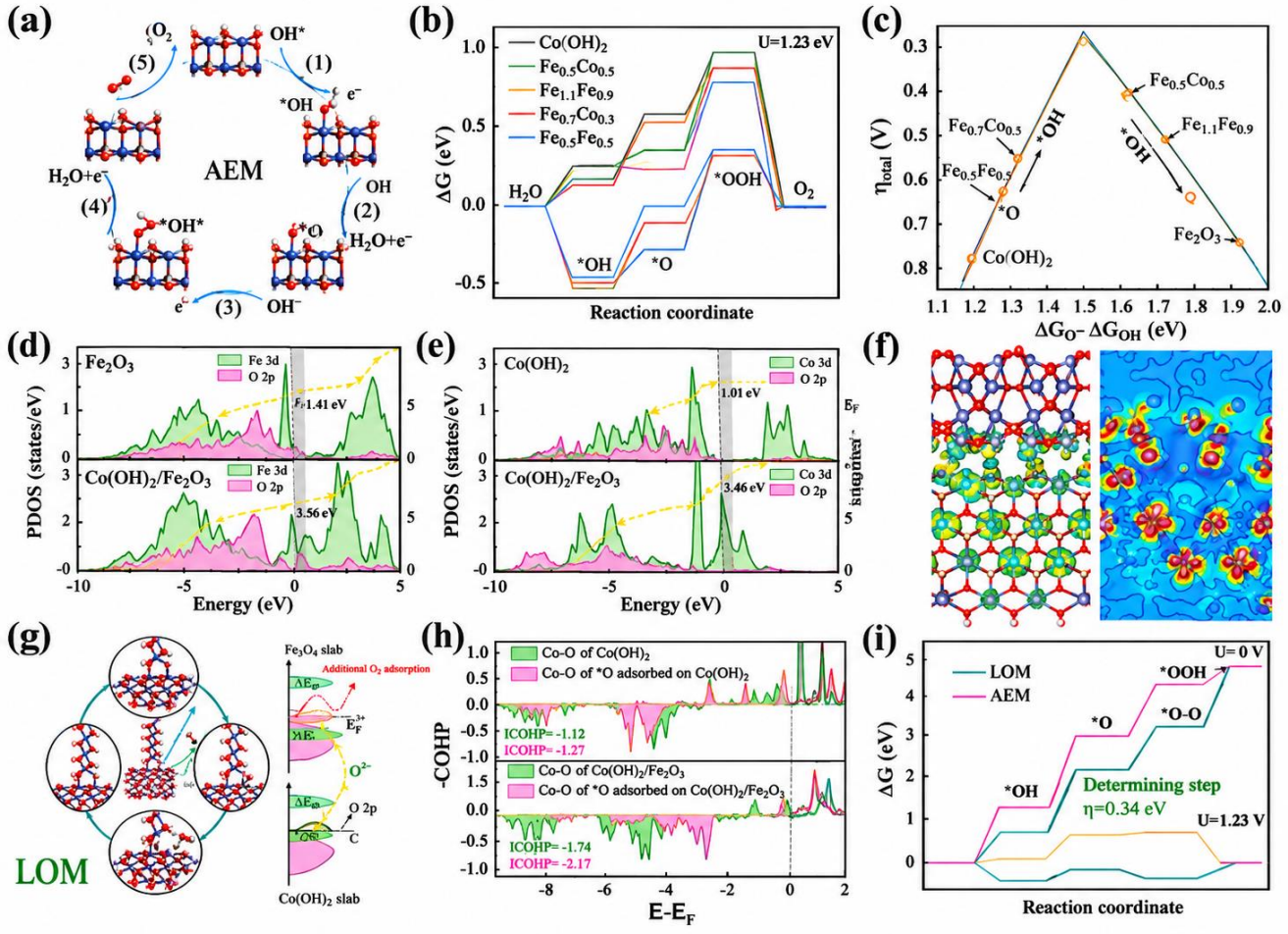


Figure 7. DFT-based investigation of the oxygen evolution reaction (OER) mechanisms and electronic properties of Fe-modified $Co(OH)_2$. (a) Schematic representation of the adsorbate evolution mechanism (AEM) proposed by Nørskov. (b) Calculated Gibbs free-energy profiles for the AEM pathway on $Co(OH)_2$ and Fe–$Co(OH)_2$. (c) Relationship between the OER overpotential and the difference in adsorption free energies, $\Delta G_{*O} - \Delta G_{*OH}$. (d, e) Projected density of states (PDOS) for Fe_2O_3 and $Co(OH)_2$, respectively. (f) Differential charge-density distribution. (g) Schematic illustration of the coupling between the AEM and lattice oxygen mechanism (LOM), together with the electronic band structures of Fe_2O_3 and $Co(OH)_2$ associated with Mott–Hubbard splitting. (h) Integrated crystal orbital Hamilton population (ICOHP) analysis. (i) Gibbs free-energy diagrams for the elementary OER steps on Fe–$Co(OH)_2$ and $Co(OH)_2$. Adapted from Xin et al. [38], with permission from Wiley. Copyright © 2025 Wiley.

Wu et al. (2022) [144] developed a magnetic type-II $ZnFe_2O_4$/ZnO aerogel heterojunction photocatalyst for the reduction of Cr(VI) to Cr(III) (Figure 8). Electron transfer from ZnO to $ZnFe_2O_4$ is thermodynamically favorable because $ZnFe_2O_4$ has a lower Fermi level. Under visible-light irradiation, electrons can subsequently transfer from $ZnFe_2O_4$ back to the conduction band of ZnO, driven by the interfacial built-in electric field. This bidirectional electron-transfer process promotes the separation of photogenerated electron–hole pairs. Furthermore, the synergistic contributions of superoxide radicals ($\bullet O_2^-$), conduction-band electrons in ZnO, and reductive carbon dioxide radical anions ($\bullet CO_2^-$) enhance the overall photocatalytic activity of the aerogel heterojunction, facilitating the reduction of Cr(VI) to Cr(III).

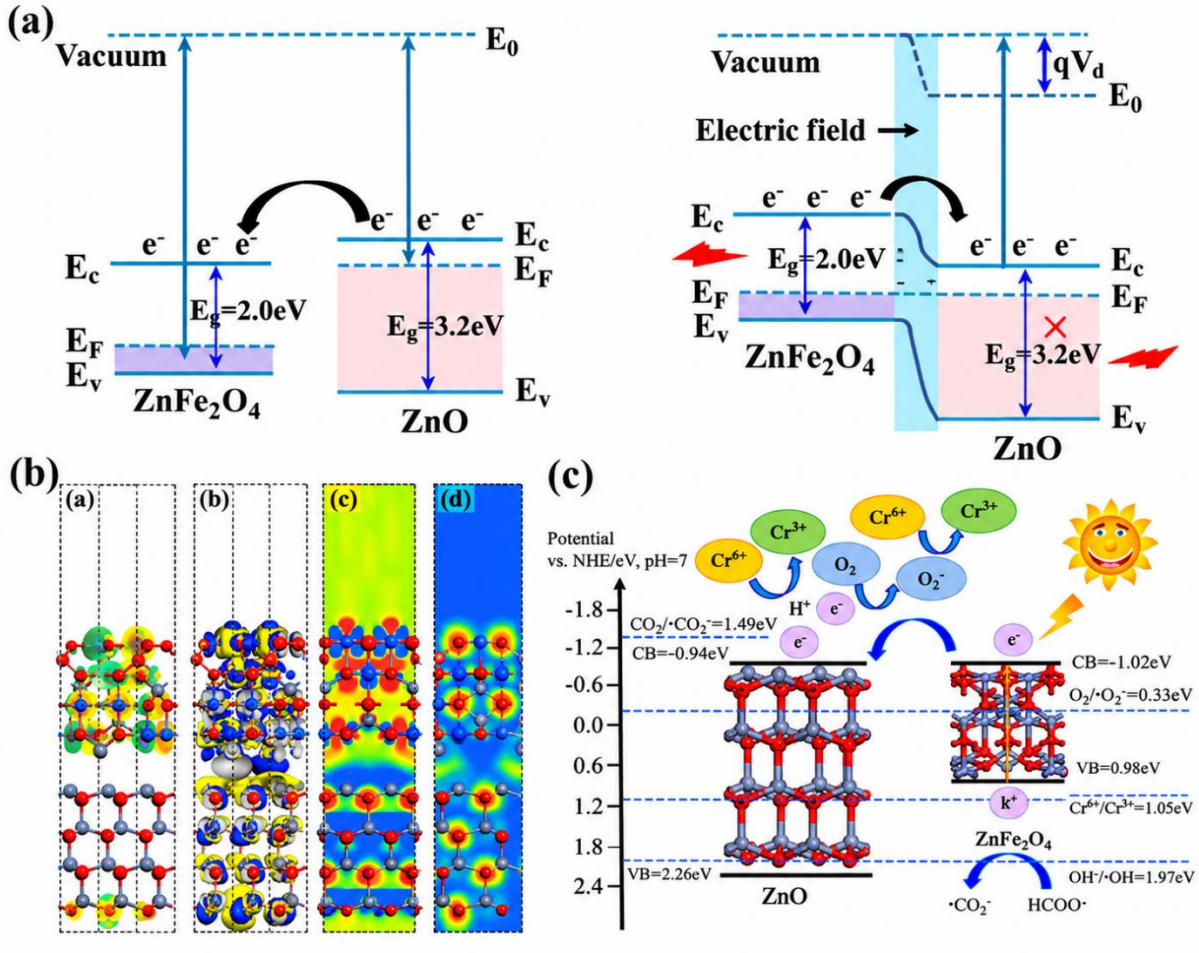


Figure 8. Interfacial charge redistribution and photocatalytic mechanism of the ZnO/$ZnFe_2O_4$ heterojunction. (a) Schematic illustration of charge redistribution at the $ZnFe_2O_4$ (110)/ZnO (001) interface before and after visible-light irradiation. (b) Spin-density distribution (red and blue denote spin-up and spin-down states, respectively), three-dimensional electron-density difference (yellow and blue indicate electron depletion and accumulation, respectively), two-dimensional electron-density difference map (red and blue represent higher and lower electron-density values, respectively), and electron localization function of the ZnO/$ZnFe_2O_4$ interface. The atomic colors represent O (red), Zn (off-white), and Fe (blue). (c) Schematic representation of the proposed photocatalytic mechanism for Cr(VI) reduction over the ZZA-400 aerogel heterojunction [144]. Adapted from Wu et al. [144], with permission from Elsevier. Copyright © 2022 Elsevier.

Yao et al. (2023) [145] investigated an electron–hole charge-transfer strategy for achieving bifunctional oxygen electrocatalysis by combining DFT calculations with electrochemical measurements of Fe_3N–$FeN_{0.0324}$ heterostructures supported on porous carbon (Fe_xN@PC). Their findings demonstrated that the formation of electron-rich and hole-rich regions at the interface can enhance both the ORR and the OER. When used as a cathode in rechargeable zinc–air batteries, Fe_xN@PC exhibited an open-circuit voltage of 1.504 V, a maximum power density of 223.67 mW cm^{-2}, and a specific capacity of 766.20 mAh g^{-1} at a current density of 5 mA cm^{-2}. The battery also maintained stable operation for more than 300 h, highlighting the potential of interfacial charge-transfer engineering for developing efficient and durable bifunctional oxygen electrocatalysts. The DFT

calculations were performed to investigate the adsorption configurations and energetics of the key oxygen-containing intermediates (*O_2, *OOH, *O, and *OH), with their optimized structures presented in Figure 9(a). The results revealed that these intermediates preferentially adsorb at the Fe_3N–$FeN_{0.0324}$ interface, where interfacial interactions promote O–O bond activation and facilitate subsequent reaction steps. The proposed charge-transfer mechanism was further elucidated through an analysis of the Fermi-level alignment of the two constituent phases and differential charge density (Figures 9(b) and 9(c)). These analyses revealed the spontaneous formation of electron-rich and hole-rich regions upon interfacial contact. Furthermore, the calculated ORR free-energy profiles at applied potentials of 0, 0.85, and 1.23 V yielded a theoretical overpotential of 0.30 V for the heterostructure (Figure 9(e)). Because the OER is the reverse of the ORR, both reactions involve the same principal oxygen-containing intermediates, resulting in closely related adsorption energetics and active-site characteristics (Figure 9(f)). Within the conventional computational framework, when both reactions proceed through the same intermediates at identical active sites, their theoretical overpotentials are constrained by the corresponding adsorption-energy relationships (Figure 9(g)). Nevertheless, the distinct electronic requirements of ORR and OER offer an opportunity to enhance bifunctional catalytic performance by spatially differentiating the active sites. Conventional ORR catalysts, including Pt-, Pd-, and M–N–C-based materials (M = Fe, Co, Ni, or Mn), generally benefit from favorable electron-transfer properties, whereas OER catalysts such as IrO_2, RuO_2, FeOOH, and NiOOH are typically associated with efficient oxidative reaction pathways. On this basis, Yao et al. proposed that electron-rich sites preferentially promote oxygen reduction, whereas hole-rich sites favor oxygen oxidation, consistent with the contrasting reduction and oxidation characteristics associated with *n*-type and *p*-type electronic behavior. In the Fe_3N–$FeN_{0.0324}$ heterostructure, $FeN_{0.0324}$ serves as the electron-rich region, facilitating electron transfer to adsorbed oxygen species and promoting subsequent proton-coupled reduction steps during ORR (Figure 9(h)). In contrast, Fe_3N acts as the hole-rich region, where the oxidative character of the surface facilitates charge transfer from adsorbed hydroxyl species and promotes deprotonation during OER (Figure 9(i)). This spatial charge separation originates from the difference in the Fermi energies of the two phases before contact. The reported values were 5.5 eV for $FeN_{0.0324}$ and 4.2 eV for Fe_3N, with the electronic structure of the latter associated with additional electrons contributed by nitrogen atoms occupying Fe lattice sites. Upon heterojunction formation, Fermi-level equilibration drives interfacial charge redistribution, establishing complementary electron-rich and hole-rich catalytic regions. These findings demonstrate that interfacial electronic-structure engineering can overcome the limitations of relying on a single type of active site and provide a theoretical foundation for designing efficient bifunctional electrocatalysts for rechargeable zinc–air batteries.

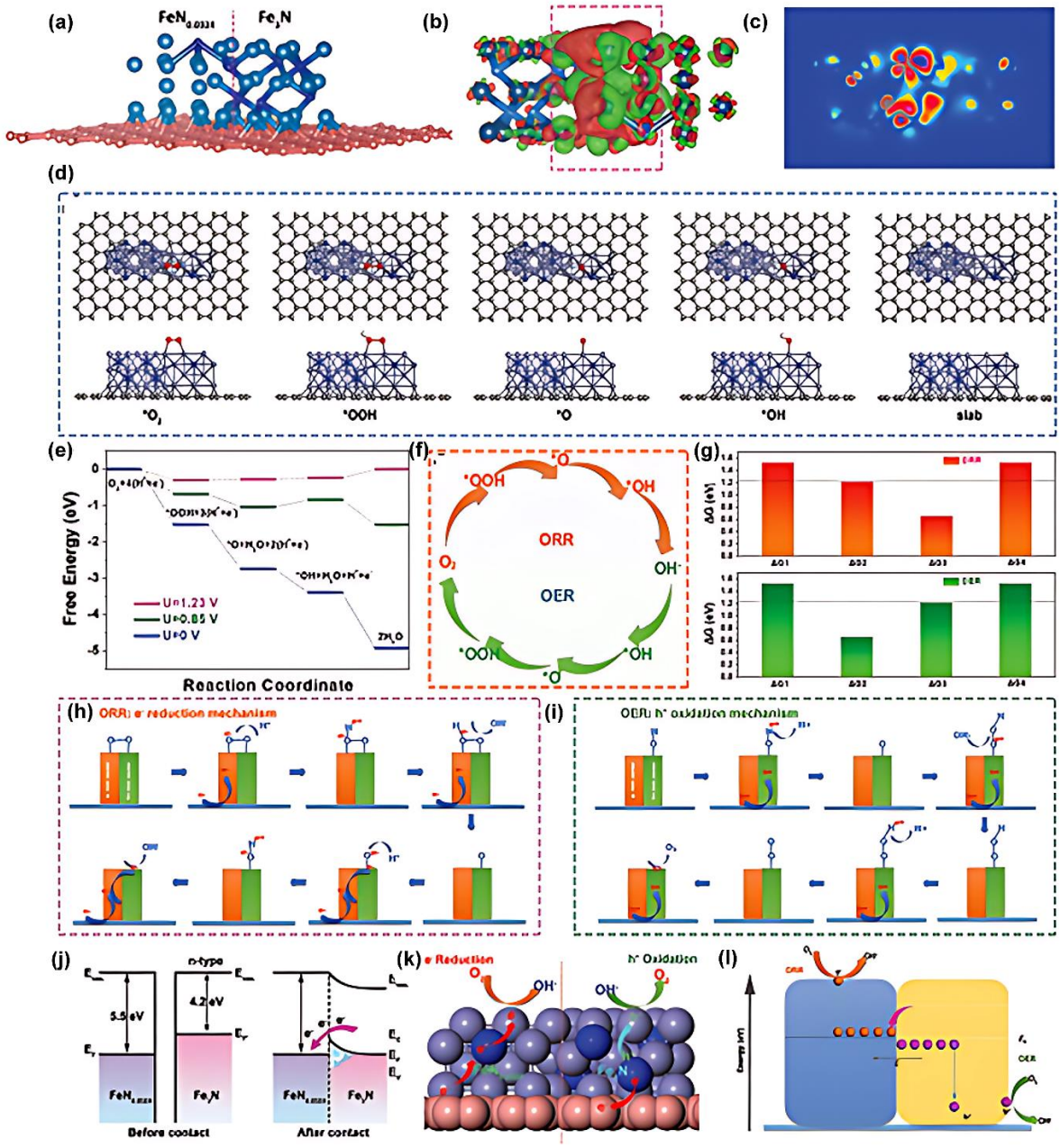


Figure 9. DFT-based analysis of interfacial electronic structure and oxygen electrocatalysis in the Fe_3N–$FeN_{0.0324}$ heterojunction supported on graphene. (a) Atomic structural model of the heterojunction. (b) Spatial distributions of electron-rich and hole-rich regions derived from DFT calculations. (c) Cross-sectional differential charge-density map, with green and orange indicating electron accumulation and depletion, respectively. (d) Proposed oxygen reduction reaction (ORR) mechanism at the FexN@PC active sites. (e) Corresponding reaction energy profiles. (f) Schematic representations of the ORR and oxygen evolution reaction (OER) pathways. (g) Calculated energy variations along the ORR and OER reaction pathways. (h, i) Proposed ORR and OER mechanisms at the FexN@PC active centers, respectively. (j) Comparison of the Fermi energy levels of the Fe_3N–$FeN_{0.0324}$ heterojunction components before and after interfacial contact. (k) Structural model and schematic illustration of the proposed ORR and OER processes at the Fe_3N–$FeN_{0.0324}$ interface. (l) Schematic energy profiles illustrating the effects of different Fermi energy levels on the electronic properties of heterojunctions [145]. Adapted from Yao et al. [145], with permission from Wiley. Copyright © 2023 Wiley.

Xiao et al. [146] investigated a photo- and magnetic-field-assisted Li–O_2 battery featuring an S-scheme MXene/In_2S_3/$CoFe_2O_4$ heterojunction photocathode designed to enhance the reversibility of oxygen electrochemistry through the combined effects of light, interfacial charge transfer, and magnetic fields. The incorporation of In_2S_3 and $CoFe_2O_4$ extends the photoresponse into the visible-light region and promotes charge-carrier separation through interfacial band alignment and the formation of a built-in electric field (Figure 10 (a) and (b)). During discharge, photogenerated electrons facilitate the ORR, whereas photogenerated holes promote the decomposition of discharge

products during charging, thereby facilitating the OER. From the perspective of semiconductor band engineering, the relative positions of the CB and VB edges are crucial for determining the thermodynamic feasibility of these reactions and for reducing the overpotential under illumination. As shown in Figures 10(c), and (d), X-ray photoelectron spectroscopy (XPS) measurements yielded valence-band energies of 1.82, 1.03, and 1.54 eV for In_2S_3, $CoFe_2O_4$, and the MXene/In_2S_3/$CoFe_2O_4$ composite, respectively. The corresponding optical band gaps, determined from Tauc plots, were 2.01, 1.54, and 1.75 eV (Figure 10(c) and (d)). These findings suggest that the semiconductor components contribute to light absorption and electron–hole pair generation, while interfacial electronic interactions modify the band structure of the composite. The comparatively higher work function of $CoFe_2O_4$ promotes interfacial charge redistribution and the establishment of an internal electric field, supporting the proposed S-scheme charge-transfer mechanism between In_2S_3 and $CoFe_2O_4$. This configuration is expected to facilitate the selective retention of strongly reducing electrons and strongly oxidizing holes, thereby enhancing the efficiency of the coupled ORR and OER processes. Furthermore, the incorporation of $CoFe_2O_4$ introduces magnetic functionality into the composite, allowing an external magnetic field to further influence charge-carrier separation and transport. The combined effects of S-scheme band alignment, interfacial electric fields, and magnetic-field assistance therefore offer a multifunctional strategy for improving the photo-assisted charge–discharge performance of Li–O_2 batteries.

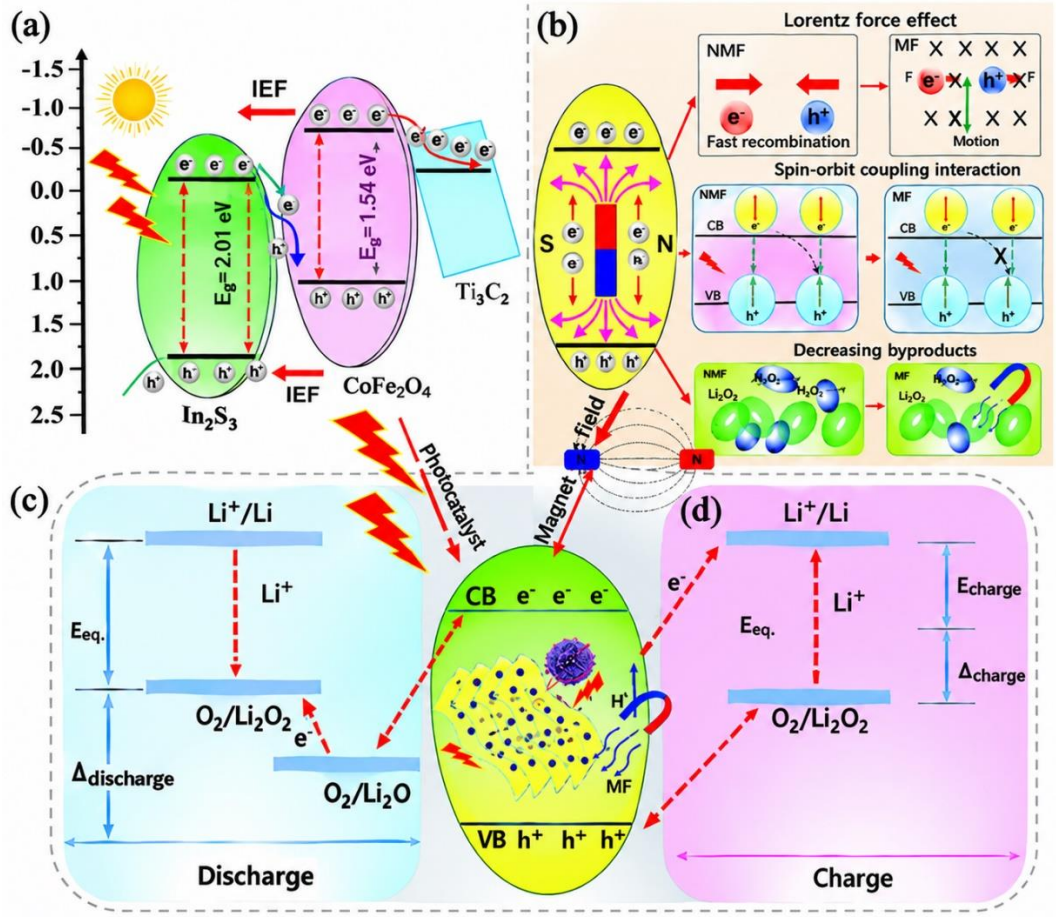


Figure 10. Work functions and valence-band electronic structures of the constituent materials and heterostructure, together with the proposed mechanisms underlying photo- and magnetically enhanced battery performance. (a–c) Calculated work functions of In_2S_3, $CoFe_2O_4$, and the TC/In_2S_3/$CoFe_2O_4$ heterostructure, respectively. (d–f) X-ray photoelectron spectroscopy (XPS) valence-band spectra of In_2S_3, $CoFe_2O_4$, and TC/In_2S_3/$CoFe_2O_4$, respectively. (g, h) Schematic illustrations of the proposed mechanisms for enhancing battery performance under photoirradiation and an applied magnetic field, respectively. (i, j) Discharge and charge profiles, respectively, of the TC/In_2S_3/$CoFe_2O_4$-based lithium–oxygen (Li–O_2) battery incorporating MXene [146]. Reprinted from Xiao et al. [146] (2024), with permission.

Mehtab et al. [147] investigated a type-II Cu_2O/g-C_3N_4 heterostructure for electrocatalytic and photocatalytic water splitting, combining experimental characterization with DFT calculations to elucidate the interfacial charge-transfer mechanism. Incorporating Cu_2O nanoparticles into g-C_3N_4 nanosheets increased the density of catalytically active sites and reduced charge-transfer resistance, thereby improving electrocatalytic performance compared with pristine g-C_3N_4. The heterostructure exhibited reported overpotentials of 47 and 72 mV for the HER and OER, respectively, with an OER Tafel slope of 72 mV dec^{-1}. Under visible-light irradiation, the Cu_2O/g-C_3N_4 composite achieved a hydrogen evolution rate of 3492 μmol g^{-1} after 5 h in the presence of triethanolamine as a sacrificial agent, nearly twice the rate obtained with pristine g-C_3N_4 (1818 μmol g^{-1}. Furthermore, the composite exhibited a Faradaic efficiency of 81% and an apparent quantum yield of 18%, highlighting its potential for solar-driven hydrogen production. The proposed charge-transfer mechanism was further investigated through DFT calculations and semiconductor band-alignment analysis. As illustrated in

Figure 11, the interface between *p*-type Cu_2O and *n*-type g-C_3N_4 establishes a type-II band alignment that facilitates the transfer of photogenerated electrons from the conduction band of Cu_2O to that of g-C_3N_4. This interfacial charge-transfer pathway promotes electron accumulation in g-C_3N_4, where the electrons participate in proton reduction to produce hydrogen. Meanwhile, triethanolamine acts as a sacrificial hole scavenger, consuming photogenerated holes and suppressing electron–hole recombination, thereby prolonging the availability of photogenerated electrons for the HER. DFT calculations further support the role of interfacial electronic coupling in facilitating stepwise electron transfer from Cu_2O to g-C_3N_4, providing a theoretical basis for the enhanced photocatalytic activity. Overall, this study highlights the importance of semiconductor junction engineering in improving charge-carrier separation, minimizing interfacial charge-transfer losses, and enhancing hydrogen production in metal oxide–carbon nitride photocatalysts.

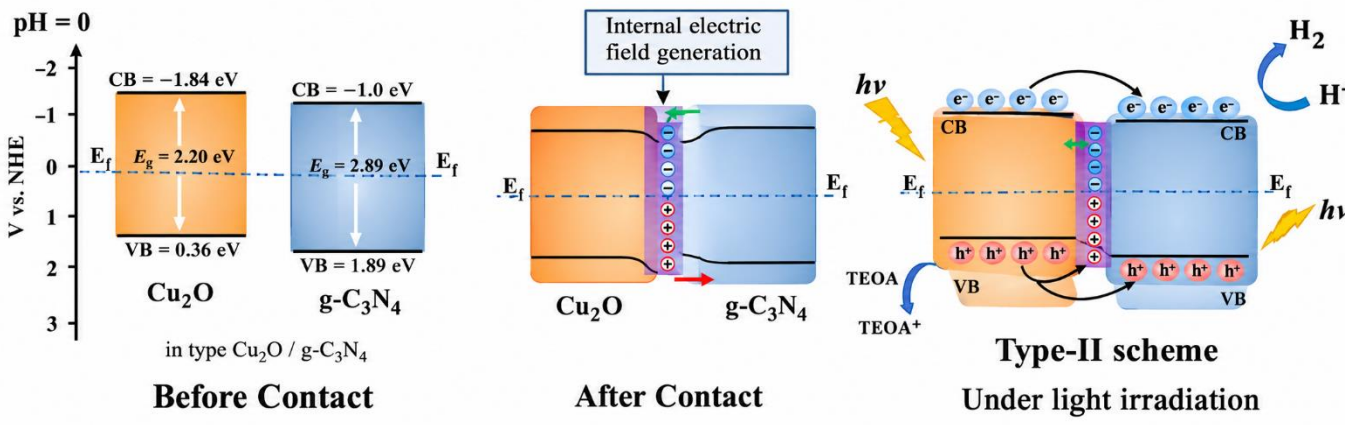


Figure 11. Schematic illustration of the type-II band alignment in a heterostructure, highlighting the interfacial charge-transfer process following heterostructure formation [147]. Adapted from Mehtab et al. [147] (2023), with permission from Elsevier.

3-2- Strain-Induced Modulation of Electronic Structure and Band Edges in Photocatalysts

Nayak and Thangavel (2023) [148] systematically investigated the structural, electronic, and photocatalytic properties of MoS_2/WS_2 heterostructures under biaxial strain for potential water-splitting applications. Among the six stacking configurations examined, conf-1 was identified as the most stable, exhibiting the lowest interlayer binding energy of −18.07 meV Å^{-2}. The MoS_2/WS_2 heterostructure exhibits type-II band alignment, with MoS_2 contributing to the conduction-band minimum (CBM) and WS_2 forming the valence-band maximum (VBM), thereby promoting effective electron–hole separation across the interface. Furthermore, the lower carrier effective masses in the heterostructure compared with those of the individual monolayers suggest enhanced carrier mobility, facilitating faster charge transport and potentially suppressing electron–hole recombination during water splitting. The MoS_2/WS_2 heterostructure also exhibits enhanced visible-light absorption, with an absorption coefficient of 8.3 × 10^5 cm^{-1}, compared with 6.33 × 10^5 cm^{-1} for the MoS_2 monolayer and 7.51 × 10^5 cm^{-1} for the WS_2 monolayer, indicating improved light-harvesting capability. Under 1% biaxial tensile strain and compressive strain of up to 4%, the CBM and VBM of the heterostructure remain suitably aligned with the water reduction and oxidation potentials, supporting its thermodynamic suitability for both the HER and the OER. In addition, tensile strain induces a moderate redshift in the absorption edge, further enhancing the heterostructure's potential for solar energy harvesting. These findings highlight the potential of two-dimensional van der Waals heterostructures (2D vdWHs) for water-splitting applications and demonstrate that their photocatalytic performance can be tuned through external strain engineering. The CBM and VBM positions of the individual MoS_2 and WS_2 monolayers, together with those of the six MoS_2/WS_2 heterostructure stacking configurations, were calculated relative to the absolute vacuum scale, as shown in Figure 12(a). The band-edge positions of both monolayers are suitably aligned with the water redox potentials, suggesting their potential as photocatalysts for water splitting. Similarly, in all six heterostructure configurations, the CBM lies above the water reduction potential (−4.44 eV), while the VBM lies below the water oxidation potential (−5.67 eV), indicating the thermodynamic feasibility of driving both the HER and OER. Furthermore, electrolyte pH plays a crucial role in determining photocatalytic performance; therefore, identifying an appropriate pH range is essential for practical applications. Accordingly, the band-edge positions were analyzed over a pH range of 0–14. The pH-dependent variation in the water redox potentials can be expressed by the following equation:

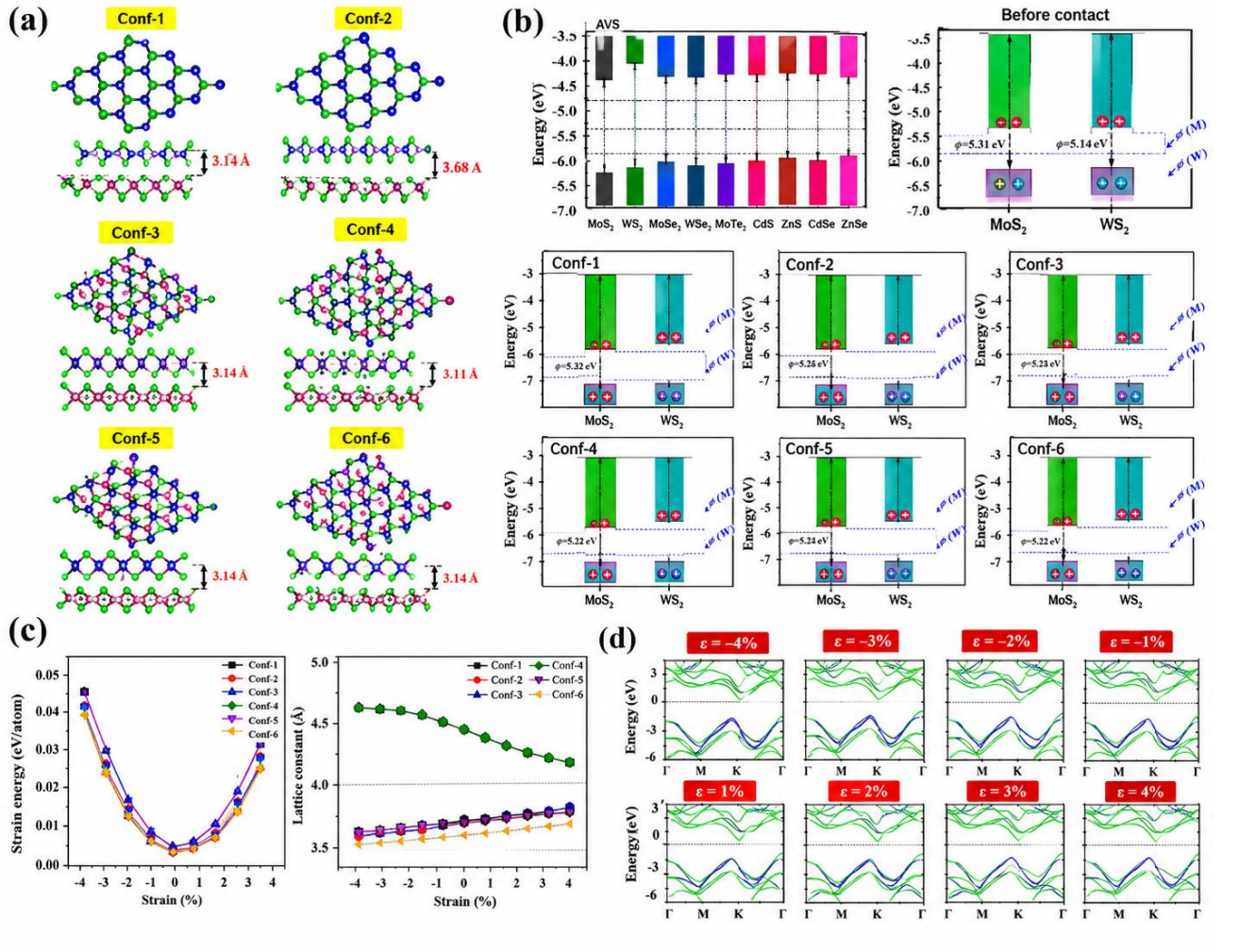


Figure 12. Structural configurations and strain-dependent electronic properties of the MoS_2/WS_2 van der Waals heterostructure. Top and side views of six distinct stacking arrangements. (a) Band-edge alignments of the isolated MoS_2 and WS_2 monolayers and the six heterostructure configurations. (b) Schematic comparison of the band alignment of the individual monolayers before interfacial contact and the corresponding heterostructures after interface formation. (c) Strain energy and conduction-band minimum (CBM) and valence-band maximum (VBM) positions of configurations conf-1, conf-4, and conf-5 under biaxial tensile and compressive strain. (d) Strain-dependent projected band structures of the conf-1 MoS_2/WS_2 heterostructure [148]. Copyright © 2023 American Chemical Society.

$$E^{red}_{H^+/H_2} = -4.44 + 0.059 \times pH \quad (16)$$

$$E^{ox}_{O_2/H_2O} = -5.67 + 0.059 \times pH$$

The conduction-band and valence-band offsets facilitate electron transfer from the CBM of WS_2 to that of MoS_2, while holes migrate from the VBM of MoS_2 to that of WS_2. The band-edge alignment of the heterostructures before and after interfacial contact is illustrated in Figures 12(b) and 12(c). Strain engineering offers an effective means of tuning the electronic, optical, photocatalytic, and charge-transport properties of 2D materials, which can accommodate substantial mechanical deformation. Consequently, applying strain to 2D vdWHs can significantly modify their functional properties. To investigate these effects in detail, the electronic properties of the most stable heterostructure, conf-1, were systematically examined under biaxial tensile and compressive strain. In addition, conf-4 and conf-5 were investigated under biaxial strain because their binding energies are comparable to that of conf-1. Biaxial strain is defined as $\varepsilon = (a-a_0)/a_0$, where a and a_0 denote the lattice constants of the strained and unstrained structures, respectively. For the two-dimensional hexagonal lattice, biaxial strain is applied uniformly along both the *x* and *y* directions, while all atomic positions within the heterostructure are fully relaxed. To evaluate the elastic response of the system, the strain energy E_s is calculated as $E_s = E_{strained} - E_{unstrained}/n$, where $E_{strained}$ and $E_{unstrained}$ are the total energies of the strained and unstrained systems, respectively, and n is the number of atoms in the unit cell. As shown in Figure 12(a), the strain energy E_s exhibits a parabolic dependence on biaxial strain, indicating that the MoS_2/WS_2 heterostructure can accommodate strain within the range of −5% to 5%. Under tensile strain, elongation of the Mo–S and W–S bonds weakens the interactions between the Mo/W and S

atoms, leading to a reduction in the band gap, defined as the energy difference between the CBM and VBM. In contrast, under compressive strain of up to 2%, the CBM shifts toward a position between the K and Γ points, whereas the VBM remains at the Γ point and retains orbital contributions similar to those of the unstrained structure. Furthermore, the valence-band edge shifts farther from the Fermi level under compressive strain, resulting in an increased band gap. Compression shortens the Mo–S and W–S bonds, strengthening the interactions between the Mo/W and S atoms and thereby widening the band gap between the CBM and VBM. However, under compressive strains of 3–4%, the VBM shifts from the Γ point to the K point. The PDOS analysis reveals that the VBM is primarily contributed by the W d_{z^2}, d_{x2-y2}, and d_{xy} orbitals, whereas the CBM is predominantly derived from the Mo d_{x2-y2} orbital. Under stronger compressive strain, the reduced coupling between these orbitals leads to a decrease in the CBM–VBM energy gap of the heterostructure.

Tang *et al*. (2024) [149] employed hybrid DFT to systematically investigate the electronic properties of g-ZnO/SnS_2, g-ZnO/$SnSe_2$, and g-ZnO/SnSSe S-scheme vdWHs under biaxial strain and external electric fields. For each g-ZnO/SnXY heterostructure, three high-symmetry stacking configurations were considered. The g-ZnO/SnSSe heterostructure is presented as a representative example in Figure 13(a–d). Among these heterostructures, g-ZnO/SnS_2 and g-ZnO/SnSSe were identified as promising photocatalysts for water splitting, exhibiting high solar-to-hydrogen conversion efficiencies under acidic and alkaline conditions, as well as under mechanical strain. The strain-induced variations in the bandgaps of g-ZnO/SnXY heterostructures are closely associated with the interplay between structural geometry and orbital hybridization within the SnXY layer. These findings provide insights into strain-induced band structure evolution in other SnXY (X, Y = S, Se) vdWHs. Interestingly, the application of an external electric field induces partially occupied nearly free-electron (NFE) states in g-ZnO/SnS_2, g-ZnO/$SnSe_2$, and g-ZnO/SnSSe. Although NFE states are generally unoccupied in most materials, which can limit their contribution to charge transport, the NFE states in g-ZnO/$SnSe_2$ exhibit particularly strong sensitivity to the external electric field. This behavior suggests that g-ZnO/$SnSe_2$ may offer potential for efficient electron transport in nanoelectronic applications.

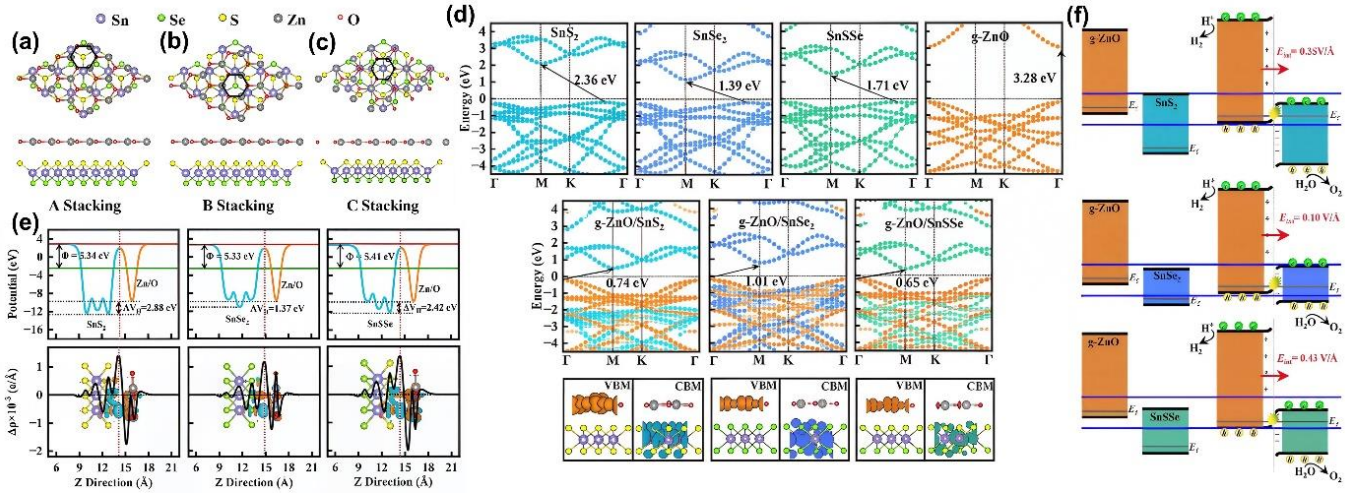


Figure 13. Structural configurations, electronic properties, and interfacial charge-transfer characteristics of g-ZnO/SnXY van der Waals heterostructures. (a–c) Top and side views of the A-, B-, and C-stacking configurations of g-ZnO/SnSSe, respectively; the hexagonal rings of g-ZnO are outlined in black. (d) HSE06-calculated band structures of the SnXY monolayers, g-ZnO monolayer, and corresponding g-ZnO/SnXY heterostructures. Band-decomposed charge-density distributions associated with the conduction-band minimum (CBM) and valence-band maximum (VBM) of g-ZnO/SnS_2, g-ZnO/$SnSe_2$, and g-ZnO/SnSSe are also shown, with an isosurface value of 4×10^{-4} e Å^{-3}. (e) Average electrostatic potential profiles of the g-ZnO/SnXY heterostructures, with red and green solid lines indicating the vacuum and Fermi levels, respectively. Planar-averaged charge-density differences and the corresponding charge-density difference maps are presented for g-ZnO/SnS_2, g-ZnO/$SnSe_2$, and g-ZnO/SnSSe. The insets show the charge-density difference isosurfaces at 4×10^{-4} e Å^{-3}, where light blue and orange represent electron accumulation and depletion, respectively; red dashed lines indicate the heterointerfaces. (f) Schematic band alignments of g-ZnO/SnS_2, g-ZnO/$SnSe_2$, and g-ZnO/SnSSe before (left) and after (right) interfacial contact. Blue lines denote the standard redox potentials for photocatalytic water splitting at pH 0 [149]. Copyright © 2024 American Chemical Society.

The HSE06-calculated E_g of monolayer SnS_2, $SnSe_2$, SnSSe, and g-ZnO are 2.36, 1.39, 1.71, and 3.28 eV, respectively (Figure 13(d)), in generally good agreement with experimentally reported values. The SnS_2, $SnSe_2$, and SnSSe monolayers exhibit indirect band gaps, with the CBM located at the M point and the VBM situated between the K and Γ points. In contrast, monolayer g-ZnO exhibits a direct band gap, with both the CBM and VBM located at the Γ point. Upon heterostructure formation, g-ZnO/SnS_2, g-ZnO/$SnSe_2$, and g-ZnO/SnSSe exhibit narrower indirect band gaps of 0.74, 1.01, and 0.65 eV, respectively. The VBM of each g-ZnO/SnXY heterostructure is primarily contributed by the g-ZnO layer, whereas the CBM predominantly originates from the SnXY component. This spatial distribution of the band-edge states is further confirmed by the band-decomposed charge density maps of the VBM and CBM shown in Figure 13(d). The CBM states are predominantly derived from the hybridization of Sn-s and S(Se)-p_x/p_y orbitals, whereas the VBM states mainly originate from O- p_x/p_y and Zn- d_{x2-y2} orbitals. Because g-ZnO has a significantly higher work function (Φ) than SnXY, electrons tend to transfer from g-ZnO to SnXY upon heterostructure formation, establishing an internal electric field

(E_{int}) directed from g-ZnO toward SnXY. The calculated work functions of the g-ZnO/SnS_2, g-ZnO/$SnSe_2$, and g-ZnO/SnSSe heterostructures are 5.34, 5.33, and 5.41 eV, respectively (Figure 13(e)). Pronounced regions of electron accumulation and depletion are observed in g-ZnO/SnS_2 and g-ZnO/SnSSe, whereas g-ZnO/$SnSe_2$ exhibits comparatively weaker charge transfer, consistent with its smaller ΔV_H. Analysis of the electronic band structures and charge-transfer characteristics of the g-ZnO/SnXY heterostructures provides a clear understanding of their band alignments. Figure 13 illustrates the band alignment diagrams of the three vdWHs. Before contact, both g-ZnO and SnXY exhibit p-type semiconducting behavior, with their Fermi levels located close to the VBM. Notably, the CBM, VBM, and Fermi level of g-ZnO are all positioned at higher energies than the corresponding levels in SnXY, satisfying a key criterion for S-scheme heterostructure formation. At pH = 0, the isolated g-ZnO monolayer can drive the H^+/H_2 reduction reaction because its CBM lies well above the reduction potential of −4.44 eV (Figure 13(f)). However, g-ZnO is unsuitable for driving the H_2O/O_2 oxidation reaction because its VBM lies above the oxidation potential of −5.67 eV. In contrast, the SnXY monolayers exhibit strong oxidation capability. Upon heterostructure formation, electrons transfer from g-ZnO to SnXY due to the difference in their Fermi levels. Consequently, g-ZnO becomes positively charged, whereas the SnXY layers accumulate electrons and become negatively charged. This interfacial charge redistribution establishes an internal electric field (E_{int}) directed from g-ZnO toward SnXY.

For the g-ZnO/SnXY heterostructures, the dependence of the band gap (E_g) on biaxial strain (ε) can be divided into several distinct regions (Figure 14(a)). The E_g -ε curves of all g-ZnO/SnXY systems exhibit a minimum at ε = -1%. In regions A and C, both tensile and compressive strains widen the band gap, primarily because the VBM remains nearly unchanged while the CBM shifts appreciably to higher energies (Figures 14(d–f)). In contrast, region B exhibits a sharp reduction in the band gap due to the previously discussed transition of the CBM from the M point to the Γ point. In region D, a transition in the band alignment type occurs in g-ZnO/$SnSe_2$ and g-ZnO/SnSSe, resulting in further bandgap narrowing. The strain-induced evolution of the band structure can be further understood by examining changes in the geometric configuration and their corresponding effects on orbital interactions, with g-ZnO/SnSSe serving as a representative example. The variations in the band gap are strongly correlated with shifts in the CBM, which is primarily derived from the SnSSe layer (Figure 14(b)). To quantify the effect of strain on interlayer charge transfer, Bader charge analysis was performed for the g-ZnO/SnXY heterostructures. The strain-dependent variation in the transferred charge closely correlates with the evolution of the band gap (Figure 14(a)). Specifically, across regions A, B, C, and D, greater interlayer electron transfer is associated with a narrower band gap. Negative transferred-charge values indicate a reversal in the direction of electron transfer, from SnXY to g-ZnO. Increased electron transfer from SnXY to g-ZnO further narrows the band gap. In this study, the strain-dependent photocatalytic performance was investigated specifically for g-ZnO/SnS_2 and g-ZnO/SnSSe. Given the strain-induced changes in band alignment in g-ZnO/SnSSe and the reversal of charge transfer in g-ZnO/SnS_2 under strong compressive strain, their photocatalytic properties were evaluated over a strain range of −5% to −9%. As the applied biaxial strain varies from −5% to 9%, the work functions of both g-ZnO/SnS_2 and g-ZnO/SnSSe increase gradually (Figure 14(g)).

The band-edge positions were compared with the standard redox potentials for H^+/H_2 reduction and O_2/H_2O oxidation, taking into account pH-dependent shifts at pH 0, 7, and 14 (Figure 14(g)). In these heterostructures, electron–hole recombination predominantly occurs between the VBM of g-ZnO and the CBM of SnXY, while the remaining electrons in the CB of g-ZnO and holes in the VB of SnXY participate in the reduction and oxidation reactions, respectively. Remarkably, over a broad pH range of 0–14 and a strain range of −5% to 9%, both g-ZnO/SnS_2 and g-ZnO/SnSSe consistently satisfy the energetic requirements for overall photocatalytic water splitting. These findings highlight the potential of these heterostructures for photocatalytic applications under challenging conditions, including highly acidic or alkaline environments and elevated pressures. The effects of an external perpendicular electric field (E_{ext}) on the electronic properties of the g-ZnO/SnXY heterostructures were also investigated. A positive external electric field ($E_{ext} > 0$) is defined as pointing from the SnXY layer toward the g-ZnO layer, as illustrated for g-ZnO/SnSSe in Figure 14(e). The influence of E_{ext} on charge transfer follows a similar trend in g-ZnO/SnS_2, g-ZnO/$SnSe_2$, and g-ZnO/SnSSe (Figure 14(i)). Specifically, a positive E_{ext} opposes the internal electric field E_{int}, initially suppressing electron transfer from g-ZnO to SnXY and eventually reversing the transfer direction at sufficiently high field strengths. Conversely, a negative E_{ext} aligns with E_{int}, thereby enhancing electron transfer from g-ZnO to SnXY. The band-gap evolution under varying external electric fields exhibits a consistent trend across all three vdWHs, as shown in Figure 14(h).

Under a negative external electric field, the band gaps of g-ZnO/SnXY gradually decrease with increasing field strength, eventually leading to a metallic state at −1.0 V $Å^{-1}$. Notably, nearly free-electron (NFE) states emerge in the g-ZnO/SnXY heterostructures when $|E_{ext}| = 0.6$ V $Å^{-1}$ and rapidly approach the Fermi level as the field strength increases. These NFE states are localized in the vacuum region beyond the material surfaces, as confirmed by the planar-averaged charge-density differences calculated under different external electric fields (Figure 14(g)). At high field strengths, pronounced peaks appear in the vacuum region, indicating the presence of these states. A stronger negative E_{ext} enhances charge accumulation within the SnXY layer, whereas an increasing positive E_{ext} initially reduces charge accumulation in this layer before subsequently increasing it, as shown in the insets of Figure 14(j). These trends are consistent with the Bader charge analysis (Figure 14(i)). Furthermore, the energies of the NFE states are closely related to the work function, as illustrated in Figure 14(j). Here, E_{NFE}-E_F denotes the energy of the lowest NFE state relative to the Fermi level. For the g-ZnO/SnXY heterostructures, increasing $|E_{ext}|$ leads to an increase in the work function and a decrease in E_{NFE}-E_F, indicating that the

NFE states shift to lower energies relative to the Fermi level. Occupied NFE states emerge in g-ZnO/SnS_2 and g-ZnO/SnSSe at $|E_{ext}| = 1.2$ V Å^{-1}, whereas they appear in g-ZnO/$SnSe_2$ at a lower field strength of $|E_{ext}| = 1.0$ V Å^{-1}.

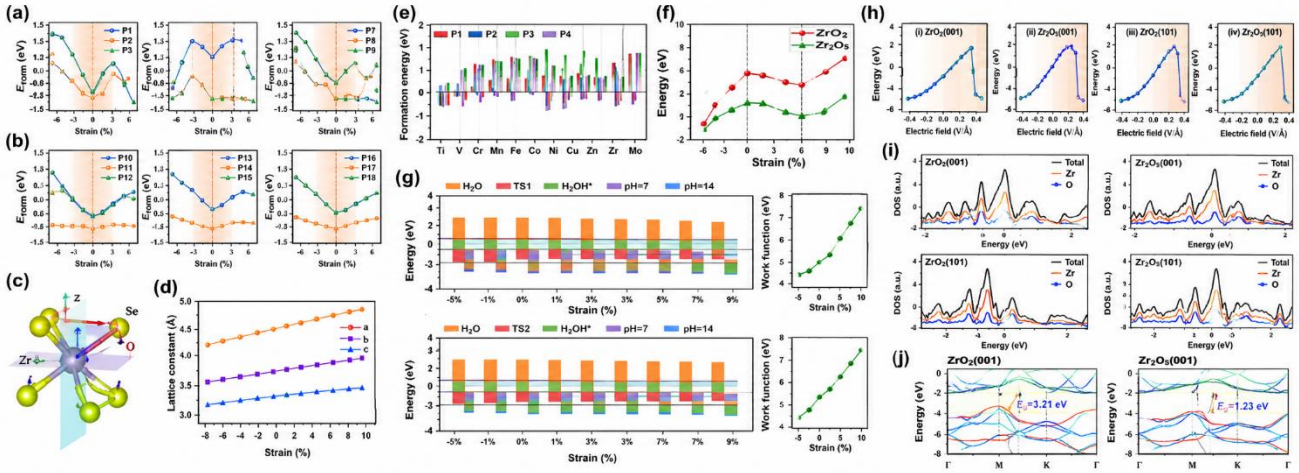


Figure 14. (a) Variation of band gaps of g-ZnO/SnXY heterostructures under different biaxial strains. (b) Evolution of CBM and VBM positions of g-ZnO/SnXY with strain, where the Fermi level is set to zero. Orange spheres represent VBM positions, and colored spheres correspond to CBM positions. (c) Atomic structure of SnSSe monolayer showing four geometric parameters: Sn-S bond length (d_1), distance between adjacent S atoms (d_2), and distances from the S atom to the xz-plane (d_3) and xy-plane (d_4) containing Sn atoms. (d) Evolution of d_1, d_2, d_3, and d_4 with applied strain. (e) Transferred charge in g-ZnO/SnXY under different strain conditions. (f) Variation of the solar-to-hydrogen (η_{STH}) efficiency with strain. (g) Band alignment evolution of g-ZnO/SnS_2, g-ZnO/$SnSe_2$, and g-ZnO/SnSSe under strain ranging from -5% to 9%. Cyan, pink, and green lines indicate the standard redox potentials for photocatalytic water splitting at pH = 0, 7, and 14, respectively. (h) Dependence of band gap on the applied electric field for g-ZnO/SnXY. (i) Variation of transferred charge in g-ZnO/SnXY under different electric field strengths, along with a schematic representation of the positive field direction. (j) Planar-averaged charge density differences of g-ZnO/SnXY under various electric fields, where E_{NEF} -E_f is shown as a function of the work function, and solid lines denote the vacuum energy level [149]. Copyright 2024, American Chemical Society.

4- Conclusion

Density functional theory (DFT) has become a cornerstone of computational materials science for probing the elementary steps of electrocatalytic and photocatalytic reactions and for the rational design of functional materials for energy conversion. As this review has shown, first-principles calculations offer atomistic-level insight into structural configurations, electronic properties, interfacial interactions, and reaction energetics. These insights make it possible to correlate intrinsic material characteristics with catalytic activity, establishing a quantitative basis for structure-property-performance relationships. Of particular importance, the evaluation of Gibbs free-energy changes (ΔG) along elementary reaction steps offers a thermodynamic framework for locating energetically demanding intermediates, comparing competing reaction pathways, and predicting catalytic activity. Computational studies of the hydrogen evolution reaction (HER), oxygen reduction reaction (ORR), and electrochemical CO_2 reduction reaction (CO_2RR) illustrate how first-principles methods can resolve mechanistic distinctions between catalytic systems and pinpoint the structural and electronic descriptors that govern selectivity and efficiency.

Beyond standard ground-state electronic-structure calculations, coupling DFT with more advanced theoretical treatments can substantially improve the description of material properties that govern catalytic behavior. Approaches such as the GW approximation, the Tran-Blaha modified Becke-Johnson (TB-mBJ) potential, and the Heyd-Scuseria-Ernzerhof (HSE06) hybrid functional furnish complementary information on quasiparticle excitation energies, band structures, and bandgaps, thereby mitigating the systematic bandgap underestimation of semi-local functionals. The choice of computational method is especially consequential for photocatalytic systems, where band-edge alignment, optical absorption characteristics, and charge-carrier dynamics determine whether light-driven reactions are thermodynamically and kinetically feasible. At the same time, the trade-off between predictive accuracy and computational cost must be weighed carefully when selecting an appropriate level of theory for a given material.

The surveyed studies further underscore that rational modification of material architecture and operating conditions offers an effective route to regulating catalytic behavior. Magnetic interactions can modulate spin-polarized electronic states and interfacial processes, whereas heterostructure construction can alter interfacial charge redistribution, electronic coupling, and band alignment. In addition, externally applied electric fields provide a further degree of control over charge transfer and electronic-state tuning, and in some systems can drive pronounced bandgap modulation or even semiconductor-to-metal transitions. The emergence and evolution of nearly free-electron (NFE) states under sufficiently strong fields further highlight the intricate coupling among electronic states, the Fermi level, and the work function in two-dimensional heterostructures. Likewise, strain engineering modifies interatomic distances, orbital hybridization, and electronic structure, thereby providing a means of tuning adsorption energetics and reaction thermodynamics. Importantly, these strategies are not mutually independent, and their synergistic implementation may afford a wider scope for controlling catalytic behavior than the optimization of any single parameter alone.

A key insight emerging from this review is that computational predictions gain considerably greater value when interpreted in conjunction with experimental evidence. DFT can pinpoint plausible active sites, rank candidate materials, and rationalize experimentally observed trends, whereas experimental characterization remains indispensable for verifying whether the predicted structures and reaction mechanisms persist under practical operating conditions. An integrated theoretical-experimental approach is therefore essential for distinguishing promising computational candidates from materials that deliver reproducible catalytic performance in realistic environments.

Overall, the continued advancement of DFT-based methodologies, coupled with systematic structural engineering and rigorous experimental validation, charts a promising course toward the rational design of electrocatalysts and photocatalysts. Future progress will hinge not only on improving the accuracy of electronic-structure calculations but also on explicitly accounting for realistic reaction environments, kinetic effects, and material stability in catalyst assessment. Incorporating these factors will enhance the predictive reliability of computational studies and facilitate the development of catalytic materials with superior activity, selectivity, durability, and energy-conversion efficiency.

5- Challenges and Future Perspectives

Notwithstanding the considerable advances achieved in computational catalysis, a number of methodological and practical bottlenecks still constrain the quantitative reliability of density functional theory (DFT) and hinder the rational translation of its predictions into catalyst design. Overcoming these shortcomings demands judicious selection of exchange-correlation functionals and related theoretical frameworks, the construction of models that faithfully capture operating reaction environments, and rigorous, systematic benchmarking of computed descriptors against experimental measurements.

5-1- Accuracy of Exchange–Correlation Functionals and Electronic Structure Descriptions

The reliability of DFT predictions is governed to a large extent by the approximation adopted for the exchange–correlation energy. Standard semilocal functionals, such as those based on the local density and generalized gradient approximations, systematically underestimate the fundamental band gaps of semiconductors. They are also frequently inadequate for describing spatially localized states, charge-transfer excitations, and strongly correlated magnetic materials, owing to the self-interaction error and the absence of derivative discontinuity. These deficiencies are especially consequential for photocatalytic systems and heterostructures, where the quantitative evaluation of band-edge alignment and interfacial electronic characteristics is a prerequisite for judging their suitability for target redox processes. Although many-body perturbation theory within the GW approximation, the Tran-Blaha modified Becke-Johnson (TB-mBJ) potential, and screened hybrid functionals such as HSE06 can ameliorate specific deficiencies of electronic-structure predictions, they differ considerably in computational overhead, theoretical scope, and transferability across material classes. Moreover, an improved description of the fundamental band gap does not necessarily translate into reliable adsorption energies, activation barriers, or free-energy profiles. Accordingly, the selection of an electronic-structure methodology should be dictated by the target property, the physicochemical nature of the system, and the availability of experimental benchmarks, rather than by band-gap agreement alone.

5-2- Modeling Realistic Electrochemical and Photocatalytic Environments

To limit computational expense, a large proportion of theoretical investigations rely on idealized surface models, isolated adsorbates, or simplified interfacial configurations. In practice, however, catalytic transformations take place in intricate environments characterized by explicit solvation, electrolyte composition, externally applied potentials, adsorbate coverage effects, and thermally induced structural fluctuations. These factors can substantially alter adsorption geometries, the thermodynamic stability of reaction intermediates, mechanistic pathways, and the relative energetics of competing reaction channels. In electrochemical systems in particular, disregarding the electrode potential and the electric field at the electrode-electrolyte interface may give rise to an incomplete, and potentially misleading, representation of the reaction energetics.

By analogy, the efficiency of a photocatalyst cannot be inferred from the computed band gap alone, since it is also governed by light-harvesting capability, photogenerated charge-carrier separation and transport, recombination dynamics, and interfacial charge transfer. Accordingly, the development of more realistic computational models that explicitly account for solvation, electrochemical potential, adsorbate coverage, and pertinent environmental conditions is essential for narrowing the discrepancy between theoretical predictions and experimentally observed behavior.

5-3- Limitations of Thermodynamic Descriptors and Reaction Mechanisms

Gibbs free-energy diagrams are extensively employed to compare competing catalytic pathways and to identify the potential-determining or rate-limiting steps. Nevertheless, thermodynamic descriptors alone are insufficient to quantitatively predict reaction rates or to rationalize product selectivity. An elementary step associated with an unfavorable free-energy change does not necessarily coincide with the step exhibiting the highest kinetic barrier, whereas reaction pathways characterized by comparable thermodynamic profiles may display markedly different activation energies. The computational hydrogen electrode (CHE) model and related thermodynamic frameworks offer a tractable means of estimating the energetics of electrochemical reactions. Their predictions, however, are contingent upon approximations regarding the electrode potential, solution pH, solvation effects, and the surface coverage of intermediates. A robust mechanistic interpretation therefore necessitates explicit consideration of activation barriers, transition-state structures, kinetic contributions, and competing reaction channels, wherever these are relevant to the system under investigation. This requirement is particularly pronounced for the HER, ORR, and CO_2RR, in which multiple intermediates and parallel pathways may coexist.

5-4- Complexity of Magnetic Heterostructures and Interfacial Charge Transfer

Magnetic materials and heterostructures present additional modeling challenges, since their physical properties are governed by spin configurations, magnetic ordering, orbital hybridization, and interlayer coupling. Distinct magnetic arrangements can give rise to markedly different electronic structures and adsorption behavior, so determining the energetically most favorable magnetic ground state is a fundamental step in any reliable computational treatment. Furthermore, the construction of heterointerfaces is frequently accompanied by lattice mismatch, structural reconstruction, point defects, and interfacial strain, each of which can modulate charge redistribution across the junction and, ultimately, the catalytic response. Bader charge partitioning and charge-density-difference analyses furnish valuable insight into electronic redistribution at surfaces and interfaces. However, such quantities should not be treated in isolation as direct indicators of catalytic activity. A rigorous assessment calls for the integration of charge-transfer descriptors with the electronic density of states, adsorption energetics, magnetic characteristics, and reaction free-energy profiles. This integrated approach is especially critical when establishing whether enhanced interfacial charge transfer genuinely promotes the catalytic process or merely reorganizes the electron density without lowering the pertinent activation barriers.

5-5- Predictive Limits of External Electric Fields and Strain Engineering

Electric-field application and lattice straining are widely recognized as theoretically accessible routes for modulating the electronic structure and catalytic reactivity of low-dimensional and heterostructured materials, although translating them into practice is far from straightforward. Simulations frequently report considerable band-gap renormalization, work-function shifts, field-driven charge accumulation, and the emergence of new electronic states. Yet at high field strengths, the associated electronic or structural responses may prove difficult to maintain under operating conditions. In particular, nearly free-electron states localized in the vacuum region call for cautious interpretation with respect to their energy position, spatial extent, and relevance to experimentally attainable phenomena. Strain-induced variation of adsorption energetics may likewise be compromised by structural instability, defect generation, or the mechanical limits of the substrate. Future work should accordingly verify the persistence and reversibility of field- and strain-induced effects, and confirm that the predicted changes lie within experimentally realizable operating regimes.

5-6- Stability, Selectivity, and Long-term Catalytic Performance

Favorable computed adsorption energies or reaction free energies do not in themselves guarantee that a catalyst will remain stable and selective during extended operation. Surface reconstruction, dissolution, oxidative degradation, defect generation, poisoning by adsorbed species, and transformations of the active phase can progressively modify catalytic behavior over time. Such deactivation processes are especially pertinent for newly proposed heterostructures and for metastable two-dimensional materials, whose structural integrity under working conditions is often uncertain. Moreover, the identification of an energetically favorable pathway for a target reaction does not by itself establish selectivity, unless competing reactions and alternative products are examined concurrently. In CO_2RR, for instance, candidate catalysts must be evaluated against the parasitic hydrogen evolution reaction and against the formation of a broad spectrum of carbon-containing products. Likewise, the ORR and other multistep processes may proceed through distinct intermediates, giving rise to different product distributions. The integration of stability assessments, competing reaction channels, and pertinent kinetic factors is therefore indispensable for attaining a more comprehensive understanding of catalytic performance.

5-7- Computational Cost and Methodological Reproducibility

High-level electronic-structure methods can be computationally prohibitive, especially for extended heterostructures, magnetic materials, defective surfaces, and reaction networks comprising numerous intermediates. Hybrid-functional and GW calculations, exhaustive configurational sampling, and explicit-solvent simulations in particular demand considerable computational resources. Such constraints often limit the number of structural configurations that can be explored, thereby introducing uncertainty into conclusions drawn from a restricted pool of candidate structures. Furthermore, discrepancies in the choice of pseudopotentials, basis-set or plane-wave energy cutoffs, Brillouin-zone sampling, convergence thresholds, initial magnetic moments, and geometry-optimization protocols can give rise to appreciable variation in the computed properties. Reproducible computational workflows should therefore specify the principal simulation parameters, demonstrate numerical convergence, state the underlying assumptions explicitly, and, wherever feasible, make the optimized structures and associated datasets openly available. Cross-validating key results against alternative theoretical methods or available experimental measurements can further strengthen the reliability of the conclusions.

5-8- Bridging Computational Predictions and Experimental Validation

A central challenge in computational catalysis lies in converting idealized theoretical predictions into experimentally reproducible gains in catalytic performance. Measured activity is frequently governed by morphology, particle size, defect populations, surface contamination, metal-support interactions, mass-transport limitations, and operating conditions that conventional DFT models do not fully capture. Conversely, experimental observations by themselves seldom permit an unambiguous assignment of the atomic-scale mechanisms underlying an observed enhancement. A synergistic combination of theory and experiment can narrow this gap: theoretical predictions can guide materials synthesis, while spectroscopic characterization and catalytic testing can, in turn, verify the proposed structures and reaction mechanisms. A meaningful comparison nevertheless requires

consistent definitions of activity metrics, appropriate reference states, and careful accounting for the experimental environment.

5-9- Future Directions

Forthcoming progress will depend on coupling high-accuracy electronic-structure methods with more faithful representations of reaction environments and with systematic experimental validation. Multiscale frameworks that integrate DFT with molecular dynamics and microkinetic modeling can bridge the gap between atomic-scale energetics and macroscopic reaction rates, thereby linking first-principles results to measurable catalytic performance. Data-driven strategies, notably machine learning, hold considerable promise for accelerating the high-throughput screening of candidate materials, provided that the underlying datasets are sufficiently diverse, computed at a consistent level of theory, and representative of the targeted chemical space. To prevent undue reliance on statistical correlations that may fail to extrapolate to unseen materials, such models should be complemented by rigorous uncertainty quantification and independent validation.

Another promising avenue is the systematic exploration of synergistic design strategies that combine magnetic ordering, heterostructure engineering, externally applied electric fields, and strain modulation. Instead of considering these degrees of freedom in isolation, future investigations could elucidate how their mutual coupling governs adsorption energetics, charge-transfer pathways, kinetic barriers, and structural stability. Special emphasis should be placed on identifying descriptors that retain their predictive reliability across diverse material families and operating regimes. Ultimately, the advancement of computational catalysis hinges on moving beyond the identification of favorable electronic properties toward holistic evaluations that integrate thermodynamics, kinetics, selectivity, stability, and experimental feasibility. Such a paradigm shift is indispensable if DFT-guided materials design is to become a more predictive and practically valuable tool for developing next-generation electrocatalysts and photocatalysts.

Conflicts of interest

There are no conflicts to declare.

References

[1] Huang, H., Zhou, S., Yu, C., Huang, H., Zhao, J., Dai, L., & Qiu, J. (2020). Rapid and energy-efficient microwave pyrolysis for high-yield production of highly-active bifunctional electrocatalysts for water splitting. *Energy & Environmental Science*, 13(2), 545–553.

[2] Liang, C., Zou, P., Nairan, A., Zhang, Y., Liu, J., Liu, K., Hu, S., Kang, F., Fan, H. J., & Yang, C. (2020). Exceptional performance of hierarchical Ni–Fe oxyhydroxide@NiFe alloy nanowire array electrocatalysts for large current density water splitting. *Energy & Environmental Science*, 13(1), 86–95.

[3] Yao, J., Huang, W., Fang, W., Kuang, M., Jia, N., Ren, H., Liu, D., Lv, C., Liu, C., & Xu, J. (2020). Promoting electrocatalytic hydrogen evolution reaction and oxygen evolution reaction by fields: Effects of electric field, magnetic field, strain, and light. *Small Methods*, 4(10), 2000494.

[4] He, S., Chen, Y., Fang, J., Liu, Y., & Lin, Z. (2025). Optimizing photocatalysis via electron spin control. *Chemical Society Reviews*, 54(5), 2154–2187.

[5] Fang, Z., Zhao, W., Shen, T., Qiu, D., Lv, Y., Hou, X., & Hou, Y. (2023). Spin-modulated oxygen electrocatalysis. *Precision Chemistry*, 1(7), 395.

[6] Chen, L., Dong, X., Wang, Y., & Xia, Y. (2016). Separating hydrogen and oxygen evolution in alkaline water electrolysis using nickel hydroxide. *Nature Communications*, 7(1), 11741.

[7] Han, N., Yang, K. R., Lu, Z., Li, Y., Xu, W., Gao, T., Cai, Z., Zhang, Y., Batista, V. S., & Liu, W. (2018). Nitrogen-doped tungsten carbide nanoarray as an efficient bifunctional electrocatalyst for water splitting in acid. *Nature Communications*, 9(1), 924.

[8] Pu, Z., Amiinu, I. S., Cheng, R., Wang, P., Zhang, C., Mu, S., Zhao, W., Su, F., Zhang, G., & Liao, S. (2020). Single-atom catalysts for electrochemical hydrogen evolution reaction: Recent advances and future perspectives. *Nano-Micro Letters*, 12(1), 21.

[9] Greeley, J., Jaramillo, T. F., Bonde, J., Chorkendorff, I. B., & Nørskov, J. K. (2006). Computational high-throughput screening of electrocatalytic materials for hydrogen evolution. *Nature Materials*, 5(11), 909–913.

[10] Batchelor, T. A. A., Pedersen, J. K., Winther, S. H., Castelli, I. E., Jacobsen, K. W., & Rossmeisl, J. (2019). High-entropy alloys as a discovery platform for electrocatalysis. *Joule*, 3(3), 834–845.

[11] Xue, K., Jiang, Y., Mofarah, S. S., Doustkhah, E., Zhou, S., Zheng, X., Huang, S., Wang, D., Sorrell, C. C., & Koshy, P. (2023). Composition-driven morphological evolution of $BaTiO_3$ nanowires for efficient piezocatalytic hydrogen production. *Chemosphere*, 338, 139337.

[12] You, B., Jiang, N., Sheng, M., Bhushan, M. W., & Sun, Y. (2016). Hierarchically porous urchin-like Ni_2P superstructures supported on nickel foam as efficient bifunctional electrocatalysts for overall water splitting. *ACS Catalysis*, 6(2), 714–721.

[13] Doustkhah, E., Esmat, M., Fukata, N., Ide, Y., Hanaor, D. A. H., & Assadi, M. H. N. (2022). MOF-derived nanocrystalline ZnO with controlled orientation and photocatalytic activity. *Chemosphere*, 303, 134932.

[14] Jiang, W.-J., Niu, S., Tang, T., Zhang, Q.-H., Liu, X.-Z., Zhang, Y., Chen, Y.-Y., Li, J.-H., Gu, L., & Wan, L.-J. (2017). Crystallinity-modulated electrocatalytic activity of a nickel (II) borate thin layer on Ni_3B for efficient water oxidation. *Angewandte Chemie*, 129(23), 6672–6677.

[15] Yoon, D., Seo, B., Lee, J., Nam, K. S., Kim, B., Park, S., Baik, H., Hoon Joo, S., & Lee, K. (2016). Facet-controlled hollow Rh_2S_3 hexagonal nanoprisms as highly active and structurally robust catalysts toward hydrogen evolution reaction. *Energy & Environmental Science*, 9(3), 850–856.

[16] Wang, M., Fu, W., Du, L., Wei, Y., Rao, P., Wei, L., Zhao, X., Wang, Y., & Sun, S. (2020). Surface engineering by doping manganese into cobalt phosphide towards highly efficient bifunctional HER and OER electrocatalysis. *Applied Surface Science*, 515, 146059.

[17] Li, P., Wang, M., Duan, X., Zheng, L., Cheng, X., Zhang, Y., Kuang, Y., Li, Y., Ma, Q., & Feng, Z. (2019). Boosting oxygen evolution of single-atomic ruthenium through electronic coupling with cobalt-iron layered double hydroxides. *Nature Communications*, 10(1), 1711.

[18] Üstünel, T., Gutiérrez Moreno, J. J., Zheng, X., Mofarah, S. S., Jahangiri, H., Kaya, S., & Doustkhah, E. (2025). Interlayer atomic voids by partial cesium defect in layered titanate activate photo

(electro)catalytic H_2 and O_2 generation. *ACS Applied Energy Materials*, 8(20), 15079–15091.

[19] Arandiyan, H., Mofarah, S. S., Sorrell, C. C., Doustkhah, E., Sajjadi, B., Hao, D., Wang, Y., Sun, H., Ni, B.-J., & Rezaei, M. (2021). Defect engineering of oxide perovskites for catalysis and energy storage: Synthesis of chemistry and materials science. *Chemical Society Reviews*, 50(18), 10116–10211.

[20] Mohammadi, S., & Shokri, A. (2025). From bandgaps formations, and electrical resistivity to energy storage capabilities of tetragonal $KNbO_3$, $NaNbO_3$, $SrSnO_3$, and $SrTiO_3$: A framework for advanced energy storage materials. *Journal of Physics and Chemistry of Solids*, 113278.

[21] Mohammadi, S., Shokri, A., & Rezaei, N. (2026). Temperature-dependent magnetoresistance and Pauli magnetic susceptibility in TM-doped $Fe(OH)_2$ LDHs: DFT insight for advanced water splitting and energy devices. *Results in Physics*, 108672.

[22] Xiong, X., Cai, Z., Zhou, D., Zhang, G., Zhang, Q., Jia, Y., Duan, X., Xie, Q., Lai, S., & Xie, T. (2018). A highly-efficient oxygen evolution electrode based on defective nickel-iron layered double hydroxide. *Science China Materials*, 61(7), 939–947.

[23] Cai, L., Cheng, W., Yao, T., Huang, Y., Tang, F., Liu, Q., Liu, W., Sun, Z., Hu, F., & Jiang, Y. (2017). High-content metallic 1T phase in MoS_2-based electrocatalyst for efficient hydrogen evolution. *The Journal of Physical Chemistry C*, 121(28), 15071–15077.

[24] El-Hosainy, H., Esmat, M., El-Sheikh, S., Hakki, A., Doustkhah, E., Tahawy, R., Ismail, A. A., El-Bery, H. M., Jevasuwan, W., & Fukata, N. (2026). Synergistic effect of oxygen vacancies and plasmonic Au nanoparticles in anatase-brookite TiO_2 for efficient solar-driven 2-methylbenzimidazole and hydrogen co-production. *Solar Energy Materials and Solar Cells*, 295, 113973.

[25] Hou, Y., Qiu, M., Kim, M. G., Liu, P., Nam, G., Zhang, T., Zhuang, X., Yang, B., Cho, J., & Chen, M. (2019). Atomically dispersed nickel–nitrogen–sulfur species anchored on porous carbon nanosheets for efficient water oxidation. *Nature Communications*, 10(1), 1392.

[26] Zhang, X., Zhang, Y.-Y., Zhang, Y., Jiang, W.-J., Zhang, Q.-H., Yang, Y.-G., Gu, L., Hu, J.-S., & Wan, L.-J. (2019). Phase-controlled synthesis of 1T-$MoSe_2$/NiSe heterostructure nanowire arrays via electronic injection for synergistically enhanced hydrogen evolution. *Small Methods*, 3(2), 1800317.

[27] Qiu, Y., Wen, Z., Jiang, C., Wu, X., Si, R., Bao, J., Zhang, Q., Gu, L., Tang, J., & Guo, X. (2019). Rational design of atomic layers of Pt anchored on Mo_2C nanorods for efficient hydrogen evolution over a wide pH range. *Small*, 15(14), 1900014.

[28] Wang, J., Yan, M., Zhao, K., Liao, X., Wang, P., Pan, X., Yang, W., & Mai, L. (2017). Field effect enhanced hydrogen evolution reaction of MoS_2 nanosheets. *Advanced Materials*, 29(7), 1604464.

[29] Garcés-Pineda, F. A., Blasco-Ahicart, M., Nieto-Castro, D., López, N., & Galán-Mascarós, J. R. (2019). Direct magnetic enhancement of electrocatalytic water oxidation in alkaline media. *Nature Energy*, 4(6), 519–525.

[30] Jansonius, R. P., Schauer, P. A., Dvorak, D. J., MacLeod, B. P., Fork, D. K., & Berlinguette, C. P. (2020). Strain influences the hydrogen evolution activity and absorption capacity of palladium. *Angewandte Chemie International Edition*, 59(29), 12192–12198.

[31] Shi, Y., Wang, J., Wang, C., Zhai, T.-T., Bao, W.-J., Xu, J.-J., Xia, X.-H., & Chen, H.-Y. (2015). Hot electron of Au nanorods activates the electrocatalysis of hydrogen evolution on MoS_2 nanosheets. *Journal of the American Chemical Society*, 137(23), 7365–7370.

[32] Li, J. (2022). Oxygen evolution reaction in energy conversion and storage: Design strategies under and beyond the energy scaling relationship. *Nano-Micro Letters*, 14(1), 112.

[33] Wang, H., Chen, J., Lin, Y., Wang, X., Li, J., Li, Y., Gao, L., Zhang, L., Chao, D., & Xiao, X. (2021). Electronic modulation of non-van der Waals 2D electrocatalysts for efficient energy conversion. *Advanced Materials*, 33(26), 2008422.

[34] Zhang, N., & Chai, Y. (2021). Lattice oxygen redox chemistry in solid-state electrocatalysts for water oxidation. *Energy & Environmental Science*, 14(9), 4647–4671.

[35] Zhai, P., Wang, C., Zhao, Y., Zhang, Y., Gao, J., Sun, L., & Hou, J. (2023). Regulating electronic states of nitride/hydroxide to accelerate kinetics for oxygen evolution at large current density. *Nature Communications*, 14(1), 1873.

[36] Zhang, N., Feng, X., Rao, D., Deng, X., Cai, L., Qiu, B., Long, R., Xiong, Y., Lu, Y., & Chai, Y. (2020). Lattice oxygen activation enabled by high-valence metal sites for enhanced water oxidation. *Nature Communications*, 11(1), 4066.

[37] Wang, X., Zhong, H., Xi, S., Lee, W. S. V., & Xue, J. (2022). Understanding of oxygen redox in the oxygen evolution reaction. *Advanced Materials*, 34(50), 2107956.

[38] Xin, S., Tang, Y., Jia, B., Zhang, Z., Li, C., Bao, R., Li, C., Yi, J., Wang, J., & Ma, T. (2023). Coupling adsorbed evolution and lattice oxygen mechanism in Fe–$Co(OH)_2$/Fe_2O_3 heterostructure for enhanced electrochemical water oxidation. *Advanced Functional Materials*, 33(45), 2305243.

[39] Wang, Z., Shang, M., Shi, W., Zheng, F., Song, D., & Tang, P. (2026). Mechanisms of magnetic field enhanced oxygen evolution reaction on electrocatalysts of different dimensionalities. *Chemical Communications* (2026).

[40] Wang, K., Yang, Q., Zhang, H., Zhang, M., Jiang, H., Zheng, C., & Li, J. (2023). Recent advances in catalyst design and activity enhancement induced by a magnetic field for electrocatalysis. *Journal of Materials Chemistry A*, 11(15), 7802–7832.

[41] Chen, Z. W., Chen, L. X., Wen, Z., & Jiang, Q. (2019). Understanding electro-catalysis by using density functional theory. *Physical Chemistry Chemical Physics*, 21(43), 23782–23802.

[42] Xu, Y., Yan, B., Zhang, H.-J., Wang, J., Xu, G., Tang, P., Duan, W., & Zhang, S.-C. (2013). Large-gap quantum spin Hall insulators in tin films. *Physical Review Letters*, 111(13), 136804.

[43] Xie, X., Ao, Z., Su, D., Zhang, J., & Wang, G. (2015). MoS_2/graphene composite anodes with enhanced performance for sodium-ion batteries: The role of the two-dimensional heterointerface. *Advanced Functional Materials*, 25(9), 1393–1403.

[44] Lin, C.-H., Rohilla, J., Kuo, H.-H., Chen, C.-Y., Mark Chang, T.-F., Sone, M., Ingole, P. P., Lo, Y.-C., & Hsu, Y.-J. (2024). Density-functional theory studies on photocatalysis and photoelectrocatalysis: Challenges and opportunities. *Solar RRL*, 8(10), 2300948.

[45] Hohenberg, P., & Kohn, W. (1964). Inhomogeneous electron gas. *Physical Review*, 136(3B), B864–B871.

[46] Kohn, W., & Sham, L. J. (1965). Self-consistent equations including exchange and correlation effects. *Physical Review*, 140(4A), A1133–A1138.

[47] Samanta, B., Morales-García, Á., Illas, F., Goga, N., Anta, J. A., Calero, S., Bieberle-Hütter, A., Libisch, F., Muñoz-García, A. B., & Pavone, M. (2022). Challenges of modeling nanostructured

materials for photocatalytic water splitting. *Chemical Society Reviews*, 51(9), 3794–3818.

[48] Hussain, S., Wang, Y., Guo, L., & He, T. (2022). Theoretical insights into the mechanism of photocatalytic reduction of CO_2 over semiconductor catalysts. *Journal of Photochemistry and Photobiology C: Photochemistry Reviews*, 52, 100538.

[49] Zhang, S., Wang, W., Hu, F., Mi, Y., Wang, S., Liu, Y., Ai, X., Fang, J., Li, H., & Zhai, T. (2020). 2D CoOOH sheet-encapsulated Ni_2P into tubular arrays realizing 1000 mA cm^{-2}-level-current-density hydrogen evolution over 100 h in neutral water. *Nano-Micro Letters*, 12(1), 140.

[50] Kresse, G., & Furthmüller, J. (1996). Efficient iterative schemes for ab initio total-energy calculations using a plane-wave basis set. *Physical Review B*, 54(16), 11169–11186.

[51] Segall, M. D., Lindan, P. J. D., Probert, M. J., Pickard, C. J., Hasnip, P. J., Clark, S. J., & Payne, M. C. (2002). First-principles simulation: Ideas, illustrations and the CASTEP code. *Journal of Physics: Condensed Matter*, 14(11), 2717–2744.

[52] Giannozzi, P., Baroni, S., Bonini, N., Calandra, M., Car, R., Cavazzoni, C., Ceresoli, D., Chiarotti, G. L., Cococcioni, M., & Dabo, I. (2009). QUANTUM ESPRESSO: A modular and open-source software project for quantum simulations of materials. *Journal of Physics: Condensed Matter*, 21(39), 395502.

[53] Delley, B. (2000). From molecules to solids with the $DMol^3$ approach. *The Journal of Chemical Physics*, 113(18), 7756–7764.

[54] Gonze, X., Beuken, J.-M., Caracas, R., Detraux, F., Fuchs, M., Rignanese, G.-M., Sindic, L., Verstraete, M., Zerah, G., & Jollet, F. (2002). First-principles computation of material properties: The ABINIT software project. *Computational Materials Science*, 25(3), 478–492.

[55] Schwarz, K., Blaha, P., & Trickey, S. B. (2010). Electronic structure of solids with WIEN2k. *Molecular Physics*, 108(21–23), 3147–3166.

[56] Luo, S., Li, T., Wang, X., Faizan, M., & Zhang, L. (2021). High-throughput computational materials screening and discovery of optoelectronic semiconductors. *Wiley Interdisciplinary Reviews: Computational Molecular Science*, 11(1), e1489.

[57] Jain, A., Shin, Y., & Persson, K. A. (2016). Computational predictions of energy materials using density functional theory. *Nature Reviews Materials*, 1(1), 15004.

[58] Heyd, J., Scuseria, G. E., & Ernzerhof, M. (2003). Hybrid functionals based on a screened Coulomb potential. *The Journal of Chemical Physics*, 118(18), 8207–8215.

[59] Tran, F., & Blaha, P. (2009). Accurate band gaps of semiconductors and insulators with a semilocal exchange-correlation potential. *Physical Review Letters*, 102(22), 226401.

[60] Tran, F., & Blaha, P. (2017). Importance of the kinetic energy density for band gap calculations in solids with density functional theory. *The Journal of Physical Chemistry A*, 121(17), 3318–3325.

[61] Friedrich, C., Betzinger, M., Schlipf, M., Blügel, S., & Schindlmayr, A. (2012). Hybrid functionals and GW approximation in the FLAPW method. *Journal of Physics: Condensed Matter*, 24(29), 293201.

[62] Pisani, C., & Dovesi, R. (1980). Exact-exchange Hartree–Fock calculations for periodic systems. I. Illustration of the method. *International Journal of Quantum Chemistry*, 17(3), 501–516.

[63] Kudin, K. N., & Scuseria, G. E. (2000). Linear-scaling density-functional theory with Gaussian orbitals and periodic boundary conditions: Efficient evaluation of energy and forces via the fast multipole method. *Physical Review B*, 61(24), 16440–16453.

[64] White, C. A., Johnson, B. G., Gill, P. M. W., & Head-Gordon, M. (1994). The continuous fast multipole method. *Chemical Physics Letters*, 230(1–2), 8–16.

[65] Burant, J. C., Scuseria, G. E., & Frisch, M. J. (1996). A linear scaling method for Hartree–Fock exchange calculations of large molecules. *The Journal of Chemical Physics*, 105(19), 8969–8972.

[66] Scuseria, G. E. (1999). Linear scaling density functional calculations with Gaussian orbitals. *The Journal of Physical Chemistry A*, 103(25), 4782–4790.

[67] Greengard, L., & Rokhlin, V. (1987). A fast algorithm for particle simulations. *Journal of Computational Physics*, 73(2), 325–348.

[68] Kutteh, R., Apra, E., & Nichols, J. (1995). A generalized fast multipole approach for Hartree–Fock and density functional computations. *Chemical Physics Letters*, 238(1–3), 173–179.

[69] Strain, M. C., Scuseria, G. E., & Frisch, M. J. (1996). Achieving linear scaling for the electronic quantum Coulomb problem. *Science*, 271(5245), 51–53.

[70] Kohn, W. (1995). Density functional theory for systems of very many atoms. *International Journal of Quantum Chemistry*, 56(4), 229–232.

[71] Schwegler, E., & Challacombe, M. (1996). Linear scaling computation of the Hartree–Fock exchange matrix. *The Journal of Chemical Physics*, 105(7), 2726–2734.

[72] Ochsenfeld, C., White, C. A., & Head-Gordon, M. (1998). Linear and sublinear scaling formation of Hartree–Fock-type exchange matrices. *The Journal of Chemical Physics*, 109(5), 1663–1669.

[73] Heyd, J., Scuseria, G. E., & Ernzerhof, M. (2003). Hybrid functionals based on a screened Coulomb potential. *The Journal of Chemical Physics*, 118(18), 8207–8215.

[74] Perdew, J. P., Ernzerhof, M., & Burke, K. (1996). Rationale for mixing exact exchange with density functional approximations. *The Journal of Chemical Physics*, 105(22), 9982–9985.

[75] Ernzerhof, M., Perdew, J. P., & Burke, K. (1997). Coupling-constant dependence of atomization energies. *International Journal of Quantum Chemistry*, 64(3), 285–295.

[76] Ernzerhof, M., & Scuseria, G. E. (1999). Assessment of the Perdew–Burke–Ernzerhof exchange-correlation functional. *The Journal of Chemical Physics*, 110(11), 5029–5036.

[77] Adamo, C., & Barone, V. (1999). Toward reliable density functional methods without adjustable parameters: The PBE0 model. *The Journal of Chemical Physics*, 110(13), 6158–6170.

[78] Perdew, J. P., Burke, K., & Ernzerhof, M. (1996). Generalized gradient approximation made simple. *Physical Review Letters*, 77(18), 3865–3868.

[79] Tao, C.-G., Yang, J., Xiang, X., & Zhao, Z.-Y. (2025). $CuCoO_2/CuMO_2$ (M = B, Al, Ga, In) delafossite isomorphous heterostructures for photocatalytic overall water splitting: Design strategy from DFT study. *Applied Surface Science*, 709, 163860.

[80] Zhao, Z., Shen, Y., Zhu, H., Zhang, Q., Zhang, Y., Yang, X., Liang, P., & Chen, L. (2023). Prediction model of type and band gap for photocatalytic g-GaN-based van der Waals heterojunction of density functional theory and machine learning techniques. *Applied Surface Science*, 640, 158400.

[81] Hedin, L. (1965). New method for calculating the one-particle Green's function with application to the electron-gas problem. *Physical Review*, 139(3A), A796–A823.

[82] Godby, R. W., Schlüter, M., & Sham, L. J. (1986). Accurate exchange-correlation potential for silicon and its discontinuity on addition of an electron. *Physical Review Letters*, 56(22), 2415–2419.

[83] Hybertsen, M. S., & Louie, S. G. (1986). Electron correlation in semiconductors and insulators: Band gaps and quasiparticle energies. *Physical Review B*, 34(8), 5390.

[84] Chawla, S., & Voth, G. A. (1998). Exact exchange in *ab initio* molecular dynamics: An efficient plane-wave-based algorithm. *The Journal of Chemical Physics*, 108(12), 4697–4700.

[85] Hamada, N., Hwang, M., & Freeman, A. J. (1990). Self-energy correction for the energy bands of silicon by the full-potential linearized augmented-plane-wave method: Effect of the valence-band polarization. *Physical Review B*, 41(6), 3620.

[86] Aryasetiawan, F. (1992). Self-energy of ferromagnetic nickel in the GW approximation. *Physical Review B*, 46(20), 13051.

[87] Ku, W., & Eguiluz, A. G. (2002). Band-gap problem in semiconductors revisited: Effects of core states and many-body self-consistency. *Physical Review Letters*, 89(12), 126401.

[88] Usuda, M., Hamada, N., Kotani, T., & van Schilfgaarde, M. (2002). All-electron GW calculation based on the LAPW method: Application to wurtzite ZnO. *Physical Review B*, 66(12), 125101.

[89] Kotani, T., & van Schilfgaarde, M. (2002). All-electron GW approximation with the mixed basis expansion based on the full-potential LMTO method. *Solid State Communications*, 121(9–10), 461–465.

[90] Yamasaki, A., & Fujiwara, T. (2002). Electronic structure of the MO oxides (M = Mg, Ca, Ti, V) in the GW approximation. *Physical Review B*, 66(24), 245108.

[91] Faleev, S. V., van Schilfgaarde, M., & Kotani, T. (2004). All-electron self-consistent GW approximation: Application to Si, MnO, and NiO. *Physical Review Letters*, 93(12), 126406.

[92] Arnaud, B., & Alouani, M. (2000). All-electron projector-augmented-wave GW approximation: Application to the electronic properties of semiconductors. *Physical Review B*, 62(7), 4464.

[93] Lebègue, S., Arnaud, B., Alouani, M., & Blöchl, P. E. (2003). Implementation of an all-electron GW approximation based on the projector augmented-wave method without plasmon pole approximation: Application to Si, SiC, AlAs, InAs, NaH, and KH. *Physical Review B*, 67(15), 155208.

[94] Shishkin, M., & Kresse, G. (2006). Implementation and performance of the frequency-dependent GW method within the PAW framework. *Physical Review B*, 74(3), 035101.

[95] Ernst, A., Henk, J., Lüders, M., Szotek, Z., & Temmerman, W. M. (2002). Quantum-size effects in ultrathin Ag films on V (001): Electronic structure and photoelectron spectroscopy. *Physical Review B*, 66(16), 165435.

[96] Saunders, V. R., Dovesi, R., Roetti, C., Causà, M., Harrison, N. M., Orlando, R., & Zicovich-Wilson, C. M. (1998). *CRYSTAL98 User's Manual*. University of Torino, Torino, Italy.

[97] Paier, J., Hirschl, R., Marsman, M., & Kresse, G. (2005). The Perdew–Burke–Ernzerhof exchange-correlation functional applied to the G2-1 test set using a plane-wave basis set. *The Journal of Chemical Physics*, 122(23).

[98] Novák, P., Kuneš, J., Chaput, L., & Pickett, W. E. (2006). Exact exchange for correlated electrons. *physica status solidi (b)*, 243(3), 563–572.

[99] Betzinger, M., Friedrich, C., & Blügel, S. (2010). Hybrid functionals within the all-electron FLAPW method: Implementation and applications of PBE0. *Physical Review B*, 81(19), 195117.

[100] Adler, S. L. (1962). Quantum theory of the dielectric constant in real solids. *Physical Review*, 126(2), 413.

[101] Friedrich, C., Betzinger, M., Schlipf, M., Blügel, S., & Schindlmayr, A. (2012). Hybrid functionals and GW approximation in the FLAPW method. *Journal of Physics: Condensed Matter*, 24(29), 293201.

[102] Perdew, J. P., Parr, R. G., Levy, M., & Balduz, J. L., Jr. (1982). Density-functional theory for fractional particle number: Derivative discontinuities of the energy. *Physical Review Letters*, 49(23), 1691.

[103] Sham, L. J., & Schlüter, M. (1983). Density-functional theory of the energy gap. *Physical Review Letters*, 51(20), 1888.

[104] Magyar, R. J., Fleszar, A., & Gross, E. K. U. (2004). Exact-exchange density-functional calculations for noble-gas solids. *Physical Review B*, 69(4), 045111.

[105] Sharma, S., Dewhurst, J. K., & Ambrosch-Draxl, C. (2005). All-electron exact exchange treatment of semiconductors: Effect of core-valence interaction on band-gap and d-band position. *Physical Review Letters*, 95(13), 136402.

[106] Kümmel, S., & Kronik, L. (2008). Orbital-dependent density functionals: Theory and applications. *Reviews of Modern Physics*, 80(1), 3–60.

[107] Heyd, J., Peralta, J. E., Scuseria, G. E., & Martin, R. L. (2005). Energy band gaps and lattice parameters evaluated with the Heyd–Scuseria–Ernzerhof screened hybrid functional. *The Journal of Chemical Physics*, 123(17).

[108] Anisimov, V. I., Zaanen, J., & Andersen, O. K. (1991). Band theory and Mott insulators: Hubbard (U) instead of Stoner (I). *Physical Review B*, 44(3), 943.

[109] Kuneš, J., Anisimov, V. I., Skornyakov, S. L., Lukoyanov, A. V., & Vollhardt, D. (2007). NiO: Correlated band structure of a charge-transfer insulator. *Physical Review Letters*, 99(15), 156404.

[110] Aulbur, W. G., Städele, M., & Görling, A. (2000). Exact-exchange-based quasiparticle calculations. *Physical Review B*, 62(11), 7121.

[111] van Schilfgaarde, M., Kotani, T., & Faleev, S. V. (2006). Adequacy of approximations in GW theory. *Physical Review B*, 74(24), 245125.

[112] Shishkin, M., Marsman, M., & Kresse, G. (2007). Accurate quasiparticle spectra from self-consistent GW calculations with vertex corrections. *Physical Review Letters*, 99(24), 246403.

[113] Tran, F., Blaha, P., & Schwarz, K. (2007). Band gap calculations with Becke–Johnson exchange potential. *Journal of Physics: Condensed Matter*, 19(19), 196208.

[114] Becke, A. D., & Johnson, E. R. (2006). A simple effective potential for exchange. *The Journal of Chemical Physics*, 124(22).

[115] Perdew, J. P., Burke, K., & Ernzerhof, M. (1998). Perdew, Burke, and Ernzerhof reply. *Physical Review Letters*, 80(4), 891.

[116] Perdew, J. P., & Wang, Y. (1992). Accurate and simple analytic representation of the electron-gas correlation energy. *Physical Review B*, 45(23), 13244.

[117] Blaha, P., Schwarz, K., Madsen, G. K. H., Kvasnicka, D., & Luitz, J. (2001). *WIEN2k: An augmented plane wave + local orbitals program for calculating crystal properties*. Vienna University of Technology, Austria.

[118] Tran, F., & Blaha, P. (2009). Accurate band gaps of semiconductors and insulators with a semilocal exchange-correlation potential. *Physical Review Letters*, 102(22), 226401.

[119] Kumari, P., Bahadur, N., Kong, L., O'Dell, L. A., Merenda, A., & Dumée, L. F. (2022). Engineering Schottky-like and heterojunction materials for enhanced photocatalysis performance: A review. *Materials Advances*, 3(5), 2309–2323.

[120] He, X., Kai, T., & Ding, P. (2021). Heterojunction photocatalysts for degradation of the tetracycline antibiotic: A review. *Environmental Chemistry Letters*, 19(6), 4563–4601.

[121] Wei, L., Yu, C., Zhang, Q., Liu, H., & Wang, Y. (2018). TiO_2-based heterojunction photocatalysts for photocatalytic reduction of CO_2 into solar fuels. *Journal of Materials Chemistry A*, 6(45), 22411–22436.

[122] Wang, H., Zhang, L., Chen, Z., Hu, J., Li, S., Wang, Z., Liu, J., & Wang, X. (2014). Semiconductor heterojunction photocatalysts: Design, construction, and photocatalytic performances. *Chemical Society Reviews*, 43(15), 5234–5244.

[123] Low, J., Yu, J., Jaroniec, M., Wageh, S., & Al-Ghamdi, A. A. (2017). Heterojunction photocatalysts. *Advanced Materials*, 29(20), 1601694.

[124] Perlman, S. S., & Feucht, D. L. (1964). PN heterojunctions. *Solid-State Electronics*, 7(12), 911–923.

[125] Mills, A., & Le Hunte, S. (1997). An overview of semiconductor photocatalysis. *Journal of Photochemistry and Photobiology A: Chemistry*, 108(1), 1–35.

[126] Trindade, T., O'Brien, P., & Pickett, N. L. (2001). Nanocrystalline semiconductors: Synthesis, properties, and perspectives. *Chemistry of Materials*, 13(11), 3843–3858.

[127] Feng, X. D., Huang, C. J., Lui, V., Khangura, R. S., & Lu, Z. H. (2005). Ohmic cathode for low-voltage organic light-emitting diodes. *Applied Physics Letters*, 86(14).

[128] Yacobi, B. G. (2003). *Semiconductor materials: An introduction to basic principles*. Springer.

[129] Mei, F., Dai, K., Zhang, J., Li, W., & Liang, C. (2019). Construction of Ag SPR-promoted step-scheme porous g-C_3N_4/Ag_3VO_4 heterojunction for improving photocatalytic activity. *Applied Surface Science*, 488, 151–160.

[130] Wang, J., Zhang, Q., Deng, F., Luo, X., & Dionysiou, D. D. (2020). Rapid toxicity elimination of organic pollutants by the photocatalysis of environment-friendly and magnetically recoverable step-scheme $SnFe_2O_4$/$ZnFe_2O_4$ nano-heterojunctions. *Chemical Engineering Journal*, 379, 122264.

[131] Jia, X., Han, Q., Zheng, M., & Bi, H. (2019). One-pot milling route to fabricate step-scheme AgI/I-BiOAc photocatalyst: Energy band structure optimized by the formation of solid solution. *Applied Surface Science*, 489, 409–419.

[132] Xu, Q., Zhang, L., Yu, J., Wageh, S., Al-Ghamdi, A. A., & Jaroniec, M. (2018). Direct Z-scheme photocatalysts: Principles, synthesis, and applications. *Materials Today*, 21(10), 1042–1063.

[133] Xu, Q., Zhang, L., Cheng, B., Fan, J., & Yu, J. (2020). S-scheme heterojunction photocatalyst. *Chem*, 6(7), 1543–1559.

[134] Li, X., Liu, J., Huang, J., He, C., Feng, Z., Chen, Z., Wan, L., & Deng, F. (2021). All-organic S-scheme heterojunction PDI-Ala/S-C_3N_4 photocatalyst with enhanced photocatalytic performance. *Acta Physico-Chimica Sinica*, 37(6), 2010030.

[135] Di, T., Xu, Q., Ho, W., Tang, H., Xiang, Q., & Yu, J. (2019). Review on metal sulphide-based Z-scheme photocatalysts. *ChemCatChem*, 11(5), 1394–1411.

[136] He, F., Meng, A., Cheng, B., Ho, W., & Yu, J. (2020). Enhanced photocatalytic H_2-production activity of WO_3/TiO_2 step-scheme heterojunction by graphene modification. *Chinese Journal of Catalysis*, 41(1), 9–20.

[137] Mu, J., Teng, F., Miao, H., Wang, Y., & Hu, X. (2020). In situ oxidation fabrication of 0D/2D SnO_2/SnS_2 novel step-scheme heterojunctions with enhanced photoelectrochemical activity for water splitting. *Applied Surface Science*, 501, 143974.

[138] Wang, R., Shen, J., Zhang, W., Liu, Q., Zhang, M., & Tang, H. (2020). Built-in electric field-induced step-scheme TiO_2/$W_{18}O_{49}$ heterojunction for enhanced photocatalytic activity under visible-light irradiation. *Ceramics International*, 46(1), 23–30.

[139] Low, J., Jiang, C., Cheng, B., Wageh, S., Al-Ghamdi, A. A., & Yu, J. (2017). A review of direct Z-scheme photocatalysts. *Small Methods*, 1(5), 1700080.

[140] Zhao, Z., Zhang, T., Yue, S., Wang, P., Bao, Y., & Zhan, S. (2024). Spin polarization: A new frontier in efficient photocatalysis for environmental purification and energy conversion. *ChemPhysChem*, 25(4), e202300726.

[141] He, S., Chen, Y., Fang, J., Liu, Y., & Lin, Z. (2025). Optimizing photocatalysis via electron spin control. *Chemical Society Reviews*, 54(5), 2154–2187.

[142] Srivastava, A., Sidler, M., Allain, A. V., Lembke, D. S., Kis, A., & Imamoğlu, A. (2015). Valley Zeeman effect in elementary optical excitations of monolayer WSe_2. *Nature Physics*, 11(2), 141–147.

[143] Wang, Z., Li, Y., Wu, C., & Tsang, S. C. E. (2022). Electric-/magnetic-field-assisted photocatalysis: Mechanisms and design strategies. *Joule*, 6(8), 1798–1825.

[144] Wu, X., Lu, J., Huang, S., Shen, X., Cui, S., & Chen, X. (2022). Facile fabrication of novel magnetic 3D $ZnFe_2O_4$/ZnO aerogel-based heterojunction for photoreduction of Cr(VI) under visible light: Controlled synthesis, facial charge distribution, and DFT study. *Applied Surface Science*, 594, 153486.

[145] Yao, Y., Wu, J., Feng, Q., Zeng, K., Wan, J., Zhang, J., Mao, B., Hu, K., Chen, L., & Zhang, H. (2023). Spontaneous internal electric field in heterojunction boosts bifunctional oxygen electrocatalysts for zinc–air batteries: Theory, experiment, and application. *Small*, 19(38), 2302015.

[146] Xiao, N., Han, P., Chen, Z., & Chen, Q. (2025). Magnetic field and photon co-enhanced S-scheme MXene/In_2S_3/$CoFe_2O_4$ heterojunction for high-performance lithium–oxygen batteries. *Journal of Colloid and Interface Science*, 680, 911–927.

[147] Mehtab, A., Mao, Y., Alshehri, S. M., & Ahmad, T. (2023). Photo/electrocatalytic hydrogen evolution using type-II Cu_2O/g-C_3N_4 heterostructure: Density functional theory addresses the improved charge transport efficiency. *Journal of Colloid and Interface Science*, 652, 1467–1480.

[148] Nayak, D., & Thangavel, R. (2023). Strain-modulated electronic and photocatalytic properties of MoS_2/WS_2 heterostructure: A DFT study. *ACS Applied Electronic Materials*, 5(1), 302–316.

[149] Tang, Y., Wang, Y., Cheng, X., & Zhang, H. (2024). Strain and electric field engineering of g-ZnO/SnXY (X, Y = S, Se) S-scheme heterostructures for photocatalyst and electronic device applications: A hybrid DFT calculation. *ACS Applied Materials & Interfaces*, 16(21), 27381–27393.